NBSIR 85-3021

OUT-OF-BAND RESPONSE OF REFLECTOR ANTENNAS

David A. Hill

National Bureau of Standards
U.S. Department of Commerce
Boulder, Colorado 80303

April 1985

¶ CAT SID: 09241 AF

Entire record displayed.

AUTH pn "HILL, DAVID A - " Record 1 of 1

LC/NACO - NAME

▸ AUTHORITY RECORD

ARN: 868884 REC STAT: REVISED ENTERED: 19830404

NAME/SUBJECT FULL EVALUATED

LC ESTABLISHED HEADING

¶

▸ 1 010 n 82208918 ¶

▸ 2 040 DGPO ‡c DLC ‡d DLC ¶

▸ 3 005 19870318174613.4 ¶

▸ 4 100 1 Hill, D. A. ‡q (David A.) [AACR2] ¶

▸ 5 500 1 Hill, David A. ¶

▸ 6 670 Gates, H.M. Technical sharing issues between broadcast-satellite and fixed services, 1982 (a.e.) ‡b t.p. (D.A. Hill) bibl. data sh. (David A. Hill, Inst. for Telecommunication Sciences, Nat. Telecommunications and Information Admin., U.S. Dept. of Commerce, Boulder, Colo.) ¶

NBSIR 85-3021

OUT-OF-BAND RESPONSE OF REFLECTOR ANTENNAS

David A. Hill

Electromagnetic Fields Division
National Engineering Laboratory
National Bureau of Standards
U.S. Department of Commerce
Boulder, Colorado 80303

April 1985

U.S. DEPARTMENT OF COMMERCE, Malcolm Baldrige, Secretary

NATIONAL BUREAU OF STANDARDS, Ernest Ambler, Director

CONTENTS

Out-of-Band Response of Reflector Antennas

David A. Hill
Electromagnetic Fields Division
National Bureau of Standards
Boulder, CO 80303

The response of reflector antennas to out-of-band frequencies has been analyzed using physical optics. A simple approximate expression has been obtained for the effective aperture, and this expression yields both the receiving pattern and the frequency dependence of the on-axis gain. The theory has been compared with published out-of-band measurements, and the pattern agreement is good, but the measured gain falls below the theory. This discrepancy is caused by mismatch loss in the coax-to-waveguide adapter, and this mismatch loss has been analyzed theoretically. The basic physical optics model for symmetrical reflectors has been extended to include offset and dual reflectors, reflector surface roughness, and transient excitation.

Key words: coax-to-waveguide adapter; effective aperture; focal region; paraboloid; physical optics; Poynting vector; out-of-band response; receiving pattern; reflector antenna.

1. Introduction

The response of antennas to out-of-band frequencies [1-3] plays an important role in interference and jamming problems. Reflector antennas are of particular interest because they are used so frequently and because they have a strong response to above-band frequencies. The analysis of reflector antennas at above-band frequencies is complicated by the presence of higher-order modes which can propagate in typical waveguide feeds. Frequencies well below the in-band frequency are not important because they are cut off by typical waveguide feeds. Consequently, "out-of-band" will refer only to above-band frequencies throughout this report.

An earlier out-of-band analysis of reflector antennas [4] yielded the radiation pattern for each propagating mode and performed a statistical analysis based on the statistics of the higher-order mode coefficients. The problem is that the statistics of the higher-order modes are highly dependent on the specific feed system and are not generally known. Such problems can be avoided by analyzing reflector antennas in the receiving mode and computing only the total received power carried by all the propagating modes. This total power is easily related to a generalized effective aperture which appears to be the most convenient receiving characteristic for out-of-band frequencies. Both the receiving pattern and the frequency response are given by the effective aperture, and the results depend only on the antenna parameters. The power which is coupled from the waveguide to the detector does of course depend on the details of the feed system, but that portion of the problem can be analyzed separately. In any case, the total power in the waveguide is a useful upper bound for the detected power.

The organization of this report is as follows. Section 2 contains an analysis of the fields and the Poynting vector in the focal region of a symmetrical paraboloid for plane-wave incidence. In Section 3, the Poynting vector is integrated over the aperture of the feed horn to yield the total received power. The integration can be done numerically or analytically, and a simple analytical approximation is adequate for most cases. The theory is compared with some earlier out-of-band measurements for frequencies from 3 GHz (in band) to 10 GHz [5], and the agreement is fairly good. Section 4 contains a number of extensions to the theoretical model, such as offset and dual reflector geometries, the effect of surface roughness, and the response of a typical coax-to-waveguide adapter. Transient excitation is also considered. Section 5 summarizes the results of this study and makes recommendations for future work.

2. Fields in the Focal Region of a Paraboloid

In this section we derive expressions for the electric and magnetic fields and the Poynting vector in the focal region of a symmetrical parabolic reflector. Much of the previous work on the focal region fields of paraboloids [6-10] was directed toward design of feed systems, and only on-axis incidence was considered. More recently, Valentino and Toulios [11] computed the electric field in the focal region of an offset paraboloid for off-axis incidence. For simplicity we consider only the symmetrical paraboloid, but we extend the previous derivation [11] to include the magnetic field and the Poynting vector for off-axis incidence.

2.1 Physical Optics Integration

The perfectly conducting, parabolic reflector is shown in figure 1. The reflector has a diameter D and a focal length f. The origin of a rectangular coordinate system (x,y,z) is located at the focus of the paraboloid. Our derivation and notation follow Valentino and Toulios [11] fairly closely, but we introduce several simplifications. Because we consider the symmetrical paraboloid, the offset angle θ_0 in [11] is zero. For the symmetrical paraboloid, without loss of generality we assume the incident plane wave is incident in the xz plane ($\phi_s = 0$ in [11]). Finally, we assume that the field point is located in the focal plane ($z_2 = 0$ or $\theta_2 = \pi/2$ in [11]).

The physical optics surface current $\underline{J}$ on the reflector is given by

$$\underline{J} = 2\,\hat{n} \times \underline{H}_i \,, \tag{1}$$

where $\hat{n}$ is the unit normal to the reflector and $\underline{H}_i$ is the incident magnetic field. For plane wave incidence, $\underline{H}_i$ is given by

$$\underline{H}_i = \underline{u}_H \, H_i \, e^{-jk\Omega_s} \,, \tag{2}$$

where k is the free space wavenumber ($=2\pi/\lambda$), λ is the wavelength, and the exp ($j\omega t$) time dependence is suppressed. In all cases, $\underline{u}$ with a subscript denotes a unit vector. We chose the quantity Ω_s to be zero at the center of the reflector, and it is given by

$$\Omega_s = \underline{u}_p \cdot \underline{r}_s \,, \tag{3}$$

where $\underline{r}_s$ is directed from the center of the reflector.

An infinitesimal surface current patch of area dS at a point P_1 on the reflector produces electric and magnetic fields [8,11] at the point P_2:

$$\begin{aligned} d\underline{E} &= \frac{-jk\eta}{4\pi}\left[\underline{J} - \underline{u}_R\,(\underline{J} \cdot \underline{u}_R)\right] \frac{e^{-jkR}}{R}\, dS \,, \\ d\underline{H} &= \frac{jk}{4\pi}\,(\underline{J} \times \underline{u}_R)\, \frac{e^{-jkR}}{R}\, dS \,, \end{aligned} \tag{4}$$

where η is the intrinsic impedance of free space. As indicated in figure 1, R is the distance between P_1 and P_2, and $\underline{u}_R$ is directed from P_1 to P_2. Also it is assumed that kR is much greater than unity.

In order to evaluate eq (4), we restrict our analysis to the region near the focus ($r_2 << r_1$). Thus we can assume that $\underline{u}_R \simeq -\underline{u}_{r_1}$ and $R \simeq r_1$ except in the phase term. The required expressions for the unit normal $\hat{n}$ and the surface differential dS have been given by Bem [12]:

$$\hat{n} = - \frac{\partial \underline{r}_1}{\partial \theta_1} \times \frac{\partial \underline{r}_1}{\partial \phi_1} \Big/ \left| \frac{\partial \underline{r}_1}{\partial \theta_1} \times \frac{\partial \underline{r}_1}{\partial \phi_1} \right|$$

and (5)

$$dS = \left| \frac{\partial \underline{r}_1}{\partial \theta_1} \times \frac{\partial \underline{r}_1}{\partial \phi_1} \right| d\theta_1 \, d\phi_1 \; .$$

Substituting eq (5) into eq (4) and carrying out some of the differentiations, we obtain

$$d\underline{E} = -j \frac{E_1}{r_1 \lambda} e^{-jk(\Omega_s + R)} (r_1^2 \sin\theta_1 \, d\phi_1 \, d\theta_1) \; \cdot$$

$$\{[(\underline{u}_{\phi_1} \cdot \underline{u}_H) + \frac{1}{r_1 \sin\theta_1} \frac{\partial r_1}{\partial \phi_1} (\underline{u}_{r_1} \cdot \underline{u}_H)] \, \underline{u}_{\theta_1} \tag{6}$$

$$-[(\underline{u}_{\theta_1} \cdot \underline{u}_H) + \frac{1}{r_1} \frac{\partial r_1}{\partial \theta_1} (\underline{u}_{r_1} \cdot \underline{u}_H)] \, \underline{u}_{\phi_1}\}$$

and

$$d\underline{H} = \frac{j \, E_1}{r_1 \lambda \eta} e^{-jk(\Omega_s + R)} (r_1^2 \sin\theta_1 \, d\phi_1 \, d\theta_1)$$

$$\{[(\underline{u}_{\theta_1} \cdot \underline{u}_H) + \frac{1}{r_1} \frac{\partial r_1}{\partial \theta_1} (\underline{u}_{r_1} \cdot \underline{u}_H)] \, \underline{u}_{\theta_1} + (\underline{u}_{\phi_1} \cdot \underline{u}_H) \, \underline{u}_{\phi_1}\} \; ,$$

where $E_i = \eta H_i$. The expression for $d\underline{E}$ agrees with previous results [11,12]. Note that $d\underline{E}$ and $d\underline{H}$ are orthogonal and both $d\underline{E}$ and $d\underline{H}$ are transverse to $\underline{u}_{r_1}$. This is consistent with the large kR assumption. The expression for R can be approximated as follows

$$R = r_1 \left[1 - 2 \frac{r_2}{r_1} \sin\theta_1 \sin\theta_2 \cos(\phi_1 - \phi_2) - 2 \frac{r_2}{r_1} \cos\theta_1 \cos\theta_2 + \frac{r_2^2}{r_1^2}\right]^{1/2} \tag{7}$$

$$\simeq r_1 - r_2 \left[\sin\theta_1 \sin\theta_2 \cos(\phi_1 - \phi_2) + \cos\theta_1 \cos\theta_2\right] .$$

In eq (7) we have neglected terms in r_2^2/r_1, and the validity of this approximation has been discussed previously [11]. The phase term Ω_s in eq (3) can be written

$$\Omega_s = (f - r_1) \cos\theta_s + r_1 \sin\theta_1 \sin\theta_s \cos\phi_1 . \tag{8}$$

Also, r_1 is given by

$$r_1 = \frac{2 f}{1 + \cos\theta_1} . \tag{9}$$

The polarization of the incident magnetic field $\underline{u}_H$ can be written

$$\underline{u}_H = a_x \underline{u}_x + a_y \underline{u}_y + a_z \underline{u}_z , \tag{10}$$

where $a_x^2 + a_y^2 + a_z^2 = 1$.

Without loss of generality, we confine the analysis to two orthogonal polarizations. For the incident magnetic field polarized in the xz plane, we have

$$a_x = \cos\theta_s, \; a_y = 0, \; a_z = -\sin\theta_s . \tag{11}$$

For the incident magnetic field polarized perpendicular to the xz plane, we have

$$a_x = 0, \; a_y = 1, \; a_z = 0 . \tag{12}$$

In order to evaluate the integration on ϕ_1 from 0 to 2π in eq (6), we take advantage of the fact that the integrands are periodic in ϕ_1. The evaluation of the ϕ_1 integrations is given in Appendix A, and the resultant expressions for $\underline{E}$ and $\underline{H}$ are

$$\underline{E} = -2\, jkE_i f \int_o^{\theta_m} e^{-jkM_o} \frac{\sin\theta_1}{1+\cos\theta_1}\, d\theta_1 \,.$$

$$\Big[\sum_{n=o}^{2} j^n J_n(kM_1)\,(C_{xn}\cos n\phi + S_{xn}\sin n\phi)\,\underline{u}_x$$

$$+\sum_{n=o}^{2} j^n J_n(kM_1)\,(C_{yn}\cos n\phi + S_{yn}\sin n\phi)\,\underline{u}_y$$

$$+\sum_{n=o}^{2} j^n J_n(kM_1)\,(C_{zn}\cos n\phi + S_{zn}\sin n\phi)\,\underline{u}_z\Big]$$

and (13)

$$\underline{H} = \frac{jkE_i f}{\eta} \int_o^{\theta_m} e^{-jkM_o} \frac{\sin\theta_1}{1+\cos\theta_1}\, d\theta_1 \,.$$

$$\Big[\sum_{n=o}^{2} j^n J_n(kM_1)\,(D_{xn}\cos n\phi + F_{xn}\sin n\phi)\,\underline{u}_x$$

$$+\sum_{n=o}^{2} j^n J_n(kM_1)\,(D_{yn}\cos n\phi + F_{yn}\sin n\phi)\,\underline{u}_y$$

$$+\sum_{n=o}^{2} j^n J_n(kM_1)\,(D_{zn}\cos n\phi + F_{zn}\sin n\phi)\,\underline{u}_z\Big] \,.$$

The upper limit θ_m of the θ_1 integration is given by [11]

$$\theta_m = \tan^{-1}(D/4\,f) \,. \tag{14}$$

All other quantities in eq (13) are defined in Appendix A.

In general, the θ_1 integration must be performed numerically, and a computer code has been written to evaluate eq (13). Note that the summations truncate at n = 2 which is in contrast to the case of the offset parabola [11,12] where the summations run to $n = \infty$.

2.2 Large f/D Approximation

When f/D is large, then θ_m as given by eq (14) is small, and small argument approximations can be used for the trigonometric functions of θ_1 . In this case, eq (13) simplifies to

$$\begin{aligned} \underline{E} &\simeq E_o \,(a_y \, \underline{u}_x - a_x \, \underline{u}_y)\, I_{\theta m} \,, \\ \underline{H} &\simeq \frac{-E_o}{\eta} \,(a_x \, \underline{u}_x - a_y \, \underline{u}_y)\, I_{\theta m} \,, \end{aligned} \tag{15}$$

where $E_o = -2jkf \, E_i e^{-jkf} \sin^2 (\theta_m/2)$,

$$I_{\theta m} = \frac{\operatorname{cosec}^2 (\theta_m/2)}{2} \int_0^{\theta_m} J_o \,(k\theta_1 P) \sin\theta_1 \, d\theta_1 \,,$$

and $P = \sqrt{(x_2 - f \sin\theta_s)^2 + y_2{}^2}$.

By setting $\sin\theta_1 \simeq \theta_1$ and $\operatorname{cosec}^2 (\theta_m/2) \simeq (2/\theta_m)^2$ in eq (15), we can evaluate $I_{\theta m}$ analytically:

$$I_{\theta m} \simeq \frac{2 \, J_1 \,(k\theta_m P)}{k\theta_m P} \,. \tag{16}$$

Note that $\underline{E}$ and $\underline{H}$ are orthogonal, and both are transverse to $\underline{u}_z$. The results in eqs (15) and (16) are consistent with earlier approximations [8,11].

A fairly simple physical picture can be obtained from eqs (15) and (16). The maximum of $I_{\theta m}$ occurs for P = 0, and this occurs for the following focal plane coordinates:

$$x_2 = f \sin\theta_s \quad \text{and} \quad y_2 = 0. \tag{17}$$

The point determined by eq (17) is essentially the geometrical optics point for a ray incident on the center of the reflector. For θ_s equal to zero the maximum fields occur at the focus, but for θ_s not equal to zero the maximum is shifted as indicated by eq (17). Away from the maximum, the decay is more rapid for higher frequencies (larger k) and also for larger reflectors (larger θ_m). Also the peak electric field E_0 is larger for higher frequencies and for larger reflectors.

2.3 Poynting Vector

The Poynting vector is of particular interest because in Section 3 we will integrate it over the aperture of the feed horn in order to determine the total received power. The real Poynting vector $\underline{S}$ is given by

$$\underline{S} = \frac{1}{2} \operatorname{Re} (\underline{E} \times \underline{H}^*) , \tag{18}$$

where Re denotes the real part and * denotes complex conjugate. A computer code has been written to evaluate eq (18) using the integral expressions for $\underline{E}$ and $\underline{H}$ in eq (13).

For large f/D, we can substitute eqs (15) and (16) into (18) to obtain the following expression

$$\underline{S} = - \frac{1}{2} \frac{|E_0|^2}{\eta} (a_y^2 + a_x^2) \left| \frac{2J_1(k\theta_m P)}{k\theta_m P} \right|^2 \underline{u}_z \tag{19}$$

For the incident magnetic field polarized in the y direction, $a_y = 1$ and $a_x = 0$. For the magnetic field polarized in the xz plane, $a_x = \cos\theta_s$ and $a_y = 0$. Since we are interested in small scan angles, we can replace $\cos\theta_s$ by unity and rewrite eq (19) as

$$\underline{S} = \underline{u}_z S_0 \left| \frac{2J_1(k\theta_m P)}{k\,\theta_m\,P} \right|^2 ,$$
$$\text{where} \quad S_0 = - \frac{1}{2} \frac{|E_0|^2}{\eta} . \tag{20}$$

Thus the approximate $\underline{S}$ is independent of the polarization of the incident field and contains only a z component S_z.

Most reflector antennas do not have large f/D ratios, but the approximation in eq (20) turns out to be surprisingly good even for relatively small values of f/D. Figure 2 shows S_z for three different values of f/D for the on-axis case $\theta_s = 0$. The curves for f/D = 1.0 and 0.4 were computed from the general integral expressions in eq (13), and the curve for f/D = ∞ was computed from eq (20). We see that the dependence on f/D is quite weak, and the large f/D approximation in eq (20) is adequate for most cases. For off-axis incidence ($\theta_s \neq 0$), eq (20) is also a good approximation, and figure 3 shows some results for f/D = 1. The large f/D curves were computed from eq (20), and the f/D = 1 curves were computed from (13) for f = 10λ and for H_y polarization. The dependence on f/λ and the incident polarization is fairly weak. Note that the agreement with the large f/D approximation is better for the smaller scan angle $\theta_s = 10^0$, but is not too bad for $\theta_s = 20^0$. We are not interested in very large θ_s because the entire physical optics method becomes questionable for θ_s too large.

3. Received Power

3.1 Feed Horn Response

Initially we consider a feed horn with an aperture of arbitrary shape. Normally feed horn aperture dimensions are on the order of a wavelength at the in-band frequency. Consequently, the aperture dimensions can be assumed to be electrically large at the higher out-of-band frequencies. Thus we make the simplifying Kirchhoff approximation that the fields in the aperture are equal to the incident fields.

If the incident fields are nonuniform, as in the focal region of a paraboloid, then the power passing through the feed horn aperture P_r is given by the integral of the Poynting vector over the aperture.

$$P_r = - \int_A S_z \, dA \; . \tag{21}$$

S_z is the z component of the incident Poynting vector, and the geometry is shown in figure 4. Since we assume that no power is dissipated in the walls of the horn and waveguide, the power propagating down the waveguide is also given by P_r in eq (21). Because the waveguide will normally be multimoded at out-of-band frequencies, P_r is the total received power in all the propagating modes. The simple theory in eq (21) does not give the individual waveguide mode amplitudes, b_n, but it gives the sum of the square of the modal amplitudes, $\sum_n |b_n|^2$, which is equal to the total power if the modes are properly normalized.

A more detailed analysis of the feed horn and the junction between the feed horn and the waveguide would be required in order to determine the individual waveguide mode coefficients. We have stayed away from this additional complexity because a knowledge of the individual mode coefficients is probably not very useful. Any waveguide bends, transitions, or irregularities would produce mode conversion and a change in the mode coefficients. Even in the uniform waveguide, the field distribution would change along the waveguide because the individual modes have different phase velocities. In contrast, the total power remains constant along the waveguide.

For the simple case where the incident field is a uniform plane wave, then S_z is simply given by

$$S_z = -S_o \cos\theta , \tag{22}$$

where S_o is the incident power density, and θ is the incidence angle shown in figure 4. In this case the integral in eq (21) is easily evaluated to yield

$$P_r = P_o \cos\theta , \quad \text{where } P_o = AS_o . \tag{23}$$

Thus we have the simple result that the receiving pattern of an electrically large receiving horn is simply $\cos\theta$ and is independent of polarization and the detailed shape of the aperture. This result only holds when we consider the total multimode power and even then is a high frequency approximation which neglects edge diffraction. If we consider the receiving pattern for an individual waveguide mode, then the pattern has a lobe structure as expected for an electrically large antenna. The specific case of an open-ended, parallel plate waveguide is analyzed in Appendix B in order to illustrate the difference between the mode patterns and the total power pattern.

3.2 Circular Aperture Integration

For a feed horn aperture of arbitrary shape, the integral for the total received power in eq (21) must be evaluated numerically. This numerical evaluation can be rather time consuming, but for the special case of a circular aperture we can obtain an analytical approximation to eq (21).

For a circular aperture of radius ρ_m, the integral in eq (21) can be written

$$P_r = - \int_0^{2\pi} \int_0^{\rho_m} S_z \rho_2 \, d\rho_2 \, d\phi_2, \tag{24}$$

where $\rho_2 = \sqrt{x_2^2 + y_2^2}$, $\phi_2 = \tan^{-1}(y_2/x_2)$, and x_2 and y_2 are the focal plane coordinates as shown in figure 1. For the general case where S_z must be determined by numerical integration, the ρ_2 and ϕ_2 integrations must also be done numerically, and a computer program has been written for this case. For large f/D, we can substitute eq (20) into eq (24) and obtain the following:

$$P_r = - S_o \int_0^{2\pi} \int_0^{\rho_m} \left[\frac{2 J_1(k\theta_m P)}{k\theta_m P} \right]^2 \rho_2 \, d\rho_2 \, d\phi_2. \tag{25}$$

First we evaluate eq (25) for axial incidence ($\theta_s = 0$). In this case, $P = \rho_2$ and the ϕ_2 integration simply yields a factor of 2π:

$$P_r = -2\pi S_o \int_0^{\rho_m} \left[\frac{2 J_1(k\theta_m \rho_2)}{k\theta_m \rho_2} \right]^2 \rho_2 \, d\rho_2. \tag{26}$$

The ρ_2 integration can be done to yield the following result:

$$P_r = P_o \left[1 - J_o^2(k\theta_m \rho_m) - J_1^2(k\theta_m \rho_m)\right], \tag{27}$$

where $P_o = \frac{|E_i|^2}{2\eta} \pi (D/2)^2$.

P_o is the total power incident on the reflector, and the factor in brackets varies from zero to unity as the quantity $k\theta_m\rho_m$ increases from zero to infinity. Both the power density S_z and the received power P_r are shown in figure 5. The ratio P_r/P_o is called aperture efficiency, and typical values for in-band reception are on the order of 50 to 90 percent.

The result in eq (27) has been given previously by Minnett and Thomas [8], but they did not treat the case of off-axis incidence ($\theta_s \neq 0$). For the case of $\theta_s \neq 0$, we lose the ϕ symmetry and must resort to an approximate integration method. Consider first the case where $f|\sin\theta_s|$ is less than ρ_m. Then the maximum intensity (or geometrical optics point) is located at $x_2 = f\sin\theta_s$ and $y_2 = 0$ inside the circle $\rho_2 = \rho_m$ as shown in figure 6. In order to do the integration analytically, we change the integration area from a circle of radius ρ_m centered at the origin to two semicircles of radii ρ_+ and ρ_- centered at the geometrical optics point as shown in figure 6. In this case, the integration can be evaluated as follows:

$$
\begin{aligned}
P_r &\approx -\pi S_o \left\{ \int_0^{\rho_+} \left[\frac{2\,J_1(k\theta_m\rho)}{k\theta_m\rho} \right]^2 \rho\, d\rho + \int_0^{\rho_-} \left[\frac{2\,J_1(k\theta_m\rho)}{k\theta_m\rho} \right] \rho\, d\rho \right\} \qquad (28) \\
&= \frac{P_o}{2} \left[2 - J_o^2(k\theta_m\rho_+) - J_1^2(k\theta_m\rho_+) - J_o^2(k\theta_m\rho_-) - J_1^2(k\theta_m\rho_-) \right],
\end{aligned}
$$

where $\rho_\pm = \rho_m \pm f\sin\theta_s$. Note that for $\theta_s = 0$, eq (28) reduces to eq (27).

For the case where $\rho|\sin\theta_s|$ is greater than ρ_m, we use a similar strategy as indicated in figure 7. In this case, the circular area is replaced by an annular sector, and the received power integral can be written

$$
\begin{aligned}
P_r &\approx -2\phi_c S_o \int_{\rho-}^{\rho+} \left[\frac{2\,J_1(k\theta_m\rho)}{k\theta_m\rho} \right]^2 \rho\, d\rho \\
&= P_o \frac{\phi_c}{\pi} \left[J_o^2(k\theta_m\rho_-) + J_1^2(k\theta_m\rho_-) - J_o^2(k\theta_m\rho_+) - J_1^2(k\theta_m\rho_+) \right],
\end{aligned} \qquad (29)
$$

where $\rho_+ = f\sin\theta_s + \rho_m$, $\rho_- = f\sin\theta_s - \rho_m$ and $\phi_c = \sin^{-1}\left(\frac{\rho_m}{f\sin\theta_s}\right)$.

It is easy to see that when $f\sin\theta_s$ is equal to ρ_m, then $\rho_- = 0$, $\phi_c = \pi/2$, and eqs (28) and (29) yield the same result for P_r. Also, it can be seen from figure 7 that eq (29) provides an upper bound for P_r because the sector includes all of the circular area and the integrand is always positive.

3.3 Effective Aperture

The effective aperture A_e is defined as the received power divided by the intensity of the incident plane wave [13]

$$A_e \equiv P_r/(|E^i|^2/2\eta) = P_r/(-S_o). \tag{30}$$

In our case we use the same definition but recognize that P_r is the received power contained in all the propagating modes. In general, A_e must be evaluated numerically because P_r must be evaluated numerically as indicated by eq (21). However, for the circular aperture we can use the approximate expressions for P_r given by eqs (28) and (29). In doing so, it is convenient to normalize A_e to the physical aperture $A_p = \pi\,(D/2)^2$. Then we can write the normalized effective aperture as

$$\frac{A_e}{A_p} = \begin{cases} \frac{1}{2}\,[2 - J_o^2(k\theta_m\rho_+) - J_1^2(k\theta_m\rho_+) - J_o^2(k\theta_m\rho_-) - J_1^2(k\theta_m\rho_-)], & f\sin\theta_s \leq \rho_m \\ \\ \frac{\phi_c}{\pi}\,[J_o^2(k\theta_m\rho_-) + J_1^2(k\theta_m\rho_-) - J_o^2(k\theta_m\rho_+) - J_1^2(k\theta_m\rho_+)], & f\sin\theta_s > \rho_m \end{cases} \tag{31}$$

where $\rho_\pm = |f\sin\theta_s \pm \rho_m|$ and ϕ_c is defined in eq (29).

It is possible to study the wide angle behavior ($f\sin\theta_s >> \theta_m$) by using the large argument approximations for the Bessel functions [14] in eq (31).

$$J_o^2(x) \approx \frac{2}{\pi x}\cos^2 x \text{ and } J_1^2(x) \approx \frac{2}{\pi x}\sin^2 x. \tag{32}$$

From eqs (31) and (32), we obtain the following asymptotic expansion for A_e/A_p

$$\frac{A_e}{A_p} \approx \frac{4\,\rho_m^{\,2}}{\pi^2 k\theta_m\,(f\sin\theta_s)^3}. \tag{33}$$

The $(\sin\theta_s)^{-3}$ dependence in eq (33) is the same as the wide angle dependence for the radiation pattern of a circular aperture of constant illumination [13]. The $\rho_m^{\,2}$ dependence is to be expected because it is proportional to the area of the receiving horn.

The angular dependence of A_e/A_p for various values of $k\theta_m\rho_m$ is shown in figure 8. The limiting case of $k\theta_m\rho_m = \infty$ corresponds to geometrical optics where the power is focused to a single spot. When $(f/\rho_m)\sin\theta_s$ is less than unity, the spot is inside the receiving horn, and A_e/A_p is unity. When (f/ρ_m) $\sin\theta_s$ is greater than unity, the spot is outside the receiving horn, and A_e/A_p is zero. For $k\theta_m\rho_m = 10$, the focused spot is smeared out, and the pattern is widened. For $k\theta_m\rho_m = 3$, the pattern is widened further. For $(f/\rho_m)\sin\theta_s$ much greater than unity, the patterns in figure 8 begin to approach the asymptotic expansion given by eq (33).

An approximate expression for the beamwidth θ_b can be obtained by setting $\theta_b/2$ equal to the incidence angle where the first zero in the J_1 Bessel function in eq (20) is located at the edge of the receiving horn. Then the Poynting vector in the receiving aperture will be small, and the integrated power and effective aperture will be small. This condition can be written

$$f\sin(\theta_b/2) = \rho_m + \rho_1, \qquad (34)$$

where $J_1(k\rho_1\theta_m) = 0$ and $k\rho_1\theta_m = \alpha_1 \approx 3.832$ represents the first zero of J_1 [14].

The above equation is easily solved for θ_b:

$$\theta_b = 2\sin^{-1}\left(\frac{\rho_m + \alpha_1/k\theta_m}{f}\right) \approx 2\,\frac{\rho_m + \alpha_1/k\theta_m}{f}. \qquad (35)$$

When k is infinite, we recover the geometrical optics result, $\sin\theta_b = 2\rho_m/f$, which is shown in figure 8. As k becomes smaller, θ_b becomes larger as shown in figure 8. For sufficiently small k, we have

$$\sin\theta_b \approx \frac{2\alpha_1}{k\theta_m f} \approx \frac{4\alpha_1}{kD} \approx \frac{2.44\lambda}{D}. \qquad (36)$$

The above result agrees with the beamwidth between the first nulls for a circular aperture with constant illumination [13].

The patterns in figure 8 were determined from the analytical approximation in eq (31). The accuracy of eq (31) has been compared with numerical integration for numerous cases. A typical comparison for f/D = 1 is shown in figure 9. The numerical integration curve was done for the incident magnetic field polarized in the y direction, while the analytical approximation is independent of the incident polarization. For the numerical integration results, there is a slight dependence on polarization. Note that the general agreement is fairly good, but that the analytical result is somewhat larger for $(f/\rho_m) \sin\theta_s$ greater than unity. This is primarily a result of the upper bound feature of the sector area approximation in figure 7. The numerical integration is time consuming because it involves triple numerical integration, over θ_1 in eq (13) and over ρ_2 and ϕ_2 in eq (24). Consequently, it is simpler and more efficient to use the analytical expression in eq (31), and this expression is adequate for most cases.

In figures 10-13, we compare the analytical approximation with previously reported experimental results [5] for frequencies from 3 GHz (the in-band frequency) to 10 GHz. The antenna tested had a diameter D of 1.22 m (4 ft) and an f/D ratio of 0.32. The small f/D ratio provided a good test for the analytical approximation which is best for large f/D. The feed horn was rectangular, 7.21 cm x 5.00 cm (2.84 in x 1.97 in) and for the theoretical comparison was modeled by a circular aperture with radius ρ_m = 3.39 cm to yield the same area. The pattern data in [5] was taken over a range of -40 to +40° in the H plane and over a smaller range (either -5 to +5° or -10 to +10°) in the E plane. Consequently, we show only the H plane comparisons in figures 10-13. The pattern comparisons are for relative power or effective aperture. Strictly speaking, the theory should not be used at the in-band frequency, 3 GHz, in figure 10 because the feed horn and waveguide are not electrically large.

A difficulty in comparing the out-of-band measurements with the theory in figures 11-13 is that the coax-to-waveguide adapter has an unknown response for multimode, out-of-band excitation. Our analysis in Section 4.5 indicates a very complicated response as a function of frequency and modal content. Because our theory yields the total power in the waveguide and the adapter has a small response for some modes and some frequencies, we can expect the theory to provide an upper bound or envelope for the detected power. This seems to be the case in figures 11-13.

In figure 14 we show the measured gain for the same antenna [5]. To convert our effective aperture A_e to gain, we divide by $\lambda^2/4\pi$, the effective aperture for an isotropic antenna [13]. Also shown is the gain result using the physical aperture A_p. The effective aperture curve is seen to gradually approach the physical aperture curve as the frequency is increased. In contrast, the measured gain becomes highly variable as the frequency is increased, and this is thought to be due to the irregular frequency response of the adapter. These measured results point out the importance of the adapter in determining what portion of the total waveguide power is actually coupled into the system.

4. Extensions to the Model

4.1 Distant Sidelobes

Because the results in the previous section are based on physical optics, the patterns are not expected to be valid for large values of θ_s. Some interesting comparisons of measured patterns and physical optics calculations for in-band frequencies have been made by Stubenrauch and Yaghjian [15]. Typically, they found that physical optics gave good accuracy for the main lobe, less accuracy for the first few sidelobes, and poor results for the distant sidelobes.

For out-of-band frequencies we are not able to calculate the details of the pattern accurately as indicated in figures 11-13, but we find that physical optics gives a reasonable estimate of the envelope pattern over the entire forward hemisphere ($\theta_s < \pi/2$). To illustrate this point, we use the geometrical theory of diffraction (GTD) to provide an estimate of the edge-diffracted field. In figure 15, a plane wave is incident on the top edge of the reflector an an angle θ_s from the axis, and we are interested in the diffracted field near the focus. If the magnetic field incident on the edge is H_i, then the diffracted field H_α at the focus is [16]

$$H_\alpha = H_i \frac{e^{-jkr_e}}{\sqrt{r_e}} D_e, \tag{37}$$

where $D_e = - \dfrac{e^{-j\pi/4}}{2\sqrt{2\pi k}} C$

and $C = \frac{1}{\cos \frac{1}{2}(\theta_{scat} - \theta_{inc})} \mp \frac{1}{\cos \frac{1}{2}(\theta_{scat} + \theta_{inc})}$.

In C, the minus sign applies to the case where the incident magnetic field is polarized parallel to the plane of incidence, and the positive sign applies to perpendicular polarization. For completeness, we could add the ray diffracted from the lower edge, but we neglect it because we are just obtaining the order of magnitude of the diffracted field. Also, we are neglecting the curvature of the diffracting edge. The angles and distance required in eq (37) are given by

$$\theta_{scat} = \frac{3\pi}{2} + \frac{\theta_m}{2}, \quad \theta_{inc} = \frac{3\pi}{2} - \frac{\theta_m}{2} - \theta_s, \quad \text{and } r_e = \frac{2f}{1 + \cos\theta_m}. \tag{38}$$

If we assume that ρ_m is much less than r_e, then the power density incident on the aperture is constant, and the z component S_z is given by

$$S_z = -\tfrac{1}{2}\eta \, |H_d|^2 \cos\theta_m. \tag{39}$$

The effective aperture A_e is then given by

$$A_e = \frac{-S_z \pi \rho_m^2}{\frac{1}{2}\eta \, |H_i|^2} = \pi \rho_m^2 D_e^2 / r_e. \tag{40}$$

If we normalize A_e by the physical aperture $A_p = \pi(D/2)^2$, and use eqs (37) and (38) in (40), we obtain

$$\frac{A_e}{A_p} = \frac{\rho_m^3}{kf^3} \cdot \frac{C^2 \cos\theta_m (1 + \cos\theta_m)^3}{64\pi \sin^2 \theta_m}. \tag{41}$$

It is interesting that the asymptotic physical optics expression (eq (33)) has the same factor $\rho_m^2/(kf^3)$, but a different angular dependence. The ρ_m^2 dependence is simply a result of A_e being proportional to the feed aperture area. The k^{-1} dependence is typical of diffracted power, and the f^{-3} dependence is a result of the A_p normalization (f^{-2} dependence) and the inverse distance (f^{-1}) dependence of the edge-diffracted power.

There is a range of incidence angle, $\pi/2 < \theta_s < \pi - \theta_m$, where the feed horn is also directly illuminated by the incident field. The geometry for this case is shown in figure 16. In this case it is easy to show that the normalized effective aperture due to direct illumination of the feed horn is

$$\frac{A_e}{A_p} = \left(\frac{2\,\rho_m}{D} \right)^2 \cos\,(\pi - \theta_s),\ \frac{\pi}{2} < \theta_s < \pi - \theta_m. \tag{42}$$

In figure 17, we show the various wide angle results for effective aperture for the reflector parameters given in figure 11. Strictly speaking, the physical optics result is not valid beyond $\theta_m/2$ (= 38°) because shadowing of the reflector takes place, but in practice it is still probably the best estimate out to θ_s = 90°. Beyond 90°, direct illumination and edge diffraction can yield a larger value of A_e. The direct illumination only extends to the shadow boundary at $\theta_s = \pi - \theta_m$ = 104°. In the vicinity of the shadow boundary, the Keller diffraction coefficients as given by eq (37) are not valid, but can be replaced by an integral form [16]. However, the maximum diffracted field is only one-half the incident field even at the shadow boundary. Note that the GTD results depend on the polarization of the incident field. Although the diffraction coefficients decrease as θ_s increases beyond 120°, there is the possibility of a backlobe at θ_s = 180° because the entire reflector rim can contribute an in-phase diffracted field.

In summary, it is probably most convenient to use the physical optics expression for θ_s < 90° and to recognize that the effective aperture can increase somewhat for θ_s > 90° because of edge diffraction or direct illumination of the feed horn. To try to obtain an accurate result for large θ_s is probably unrealistic because the results depend on the construction details (struts, reflector edge, etc.) of the antenna. Based on a large number of radiation patterns, the CCIR [17] uses the isotropic value ($A_e = \lambda^2/4\pi$) for reflector antennas at large angles for interference calculations.

4.2 Transient Fields

When a transient wave is incident on the reflector antenna, the waveform undergoes dispersion. If the frequency spectrum of the incident waveform is known, then the problem can be analyzed in the frequency domain, and the final result can be transformed to the time domain. Another approach is to obtain the impulse response of the reflector and to convolve the incident waveform with the impulse response. This method has the advantage that the impulse response can often yield a useful physical interpretation. Also, the duration of the impulse response provides an estimate of the pulse stretching which occurs when the impulse response is convolved with an incident pulse. In this section we obtain a simple approximate expression for the impulse response of the reflector, but do not attempt to analyze the effect of the feed horn or the waveguide feed.

In eqs (15) and (16), the approximate expressions are given for $\underline{E}$ and $\underline{H}$ in the focal region. For the approximations made in eqs (15) and (16), the polarizations of $\underline{E}$ and $\underline{H}$ are the same as their incident polarizations and the ratio of E to H is the free space impedance η. Thus it is sufficient to treat the scalar problem for either E or H, and the polarization factors in eq (15) can be ignored. Thus we can write the electric field spectrum as

$$E(\omega) = E_0 \frac{2\, J_1(k\theta_m P)}{k\theta_m P}, \qquad (43)$$

where $E_0 = -2jkf\, E^i(\omega)\, e^{-jkf} \sin^2(\theta_m/2)$ and P is defined in eq (15) as the distance from the geometrical optics point ($x_2 = f \sin\theta_s$, $y_2 = 0$). $E^i(\omega)$ is the spectrum of the incident waveform, and for impulse excitation $E^i(\omega)$ is unity. By setting $E^i(\omega) = 1$, making the small θ_m approximation, and writing J_1 in terms of the modified Bessel function I_1 [3.2], we can rewrite eq (43)

$$E(\omega) \approx \frac{-D\,\theta_m}{2P} I_1(j\omega b)\, e^{-j\omega f/c}, \qquad (44)$$

where $b = P\theta_m/c$.

The impulse response $\tilde{E}(t)$ is the inverse Fourier transform of eq (44)

$$\tilde{E}(t) = F^{-1}[E(\omega)] = \frac{1}{2\pi} \int_{-\infty}^{\infty} E(\omega)\, e^{j\omega t} d\omega. \qquad (45)$$

The inverse transform of $I_1(j\omega b)$ can be found in Laplace transform ($s = j\omega$) tables [18]

$$F^{-1}[I_1(j\omega b)] = \begin{cases} \dfrac{-t}{\pi b \sqrt{b^2 - t^2}}, & |t| < b \\ 0, & |t| > b. \end{cases} \qquad (46)$$

The exponential factor in eq (44) introduces a time delay, f/c, because the phase reference was taken as the center of the reflector. Consequently, $\tilde{E}(t)$ can be written

$$\tilde{E}(t) = \frac{cD}{2\pi P^2} \tilde{E}_n(\tau), \tag{47}$$

where $\tilde{E}_n(\tau) = \begin{cases} \dfrac{\tau/b}{\sqrt{(\tau/b)^2 - 1}} & , |\tau| < b \\ 0 & , |\tau| > 0 \end{cases}$

and $\tau = t - f/c$.

Thus the approximate impulse response has a finite time width w given by

$$w = 2b = \frac{2\, P\, \theta_m}{c} = \frac{2\, \theta_m \sqrt{(x_2 - f \sin\theta_s)^2 - y_2{}^2}}{c}. \tag{48}$$

The shape of the normalized impulse response $\tilde{E}_n(\tau)$ is shown in figure 18. The singularities at $\tau = \pm b$ are integrable square root singularities and present no difficulty in convolving $\tilde{E}(t)$ with any realistic incident waveform.

When P is zero, both eqs (44) and (47) are indeterminate. However, if we take the limit of P approaching zero, eq (44) becomes

$$E(\omega) \approx - \frac{D\, \theta_m}{4c} j\omega\, e^{-j\omega f/c}, \; P = 0. \tag{49}$$

The inverse transform of $j\omega$ [19] is the unit doublet, $\delta'(t)$, and the inverse transform of eq (49) is

$$\tilde{E}(t) \approx - \frac{D\theta_m}{4C} \delta'(\tau), \; P = 0. \tag{50}$$

When the doublet eq (50) is convolved with an incident waveform, the incident waveform is differentiated [19].

From eq (48) we see that the width of the impulse response is proportional to P, the distance from the geometrical optics point. For on-axis incidence ($\theta_s = 0$), the most distant points of interest are at the edge of the circular aperture, $P = \rho_m$. As an example, consider the parameters in figures 10-14: $\theta_m = 1.326$ and $\rho_m = 3.39$ cm. In this case, eq (48) yields a pulse width $w = 0.3$ ns. However, if we consider off-axis incidence, then P can be much larger. If we again consider the antenna parameters from figures 10-15 ($f = 39$ cm and $\theta_m = 1.326$), an off-axis incidence angle of $\theta_s = 30°$ yields a pulse width of $w = 1.73$ ns at the center of the aperture ($x_2 = y_2 = 0$).

It should be stressed that the results in this section are based on physical optics and are not valid at low frequencies. This means that the transient results in eqs (47) and (50) are not valid for large times. However, if the incident waveform has very little low frequency content, the convolution results should still be fairly accurate. The problem of dispersion caused by the feed horn and the waveguide has not been addressed, and such results would depend on the detailed geometry of the horn and guide. Dispersion in waveguides has been studied by inverse transforms of the modal series [20] for the acoustic problem, and the same technique would be valid for the electromagnetic problem.

4.3 Reflector Roughness

The analysis in this report has assumed a smooth parabolic reflector, and this assumption is valid when the tolerance of the reflector surface is sufficiently small in terms of the wavelength. The effect of surface roughness has been studied in the classic paper of Ruze [21] and in more recent theoretical papers [22,23]. In general, the problem is very complicated, but we can make use of the simple expression from Ruze [21]. By a statistical analysis of the physical optics integral, Ruze derived the following expression for the radiation pattern $G(\theta,\phi)$:

$$G(\theta,\phi) = G_o(\theta,\phi)\, e^{-\overline{\delta^2}} + G_s(\theta,\phi), \tag{51}$$

where G_o is the radiation pattern of the smooth reflector, $\overline{\delta^2}$ is the mean square phase error over the reflector aperture, and G_s is a scatter term which is normally negligible in the vicinity of the main beam. The mean square phase error is given by

$$\overline{\delta^2} = (4\pi\varepsilon/\lambda)^2, \tag{52}$$

where ε is defined as the effective reflector tolerance. For large f/D, ε is approximately equal to the reflector tolerance measured normal to the surface, and for smaller f/D the effective tolerance ε is somewhat less than the normal surface tolerance [21].

For cases where the second term in eq (51) is negligible, the effect of reflector roughness is simply given by the exponential factor in eq (51). Thus we can define a roughness loss L (the ratio of G_0 to G):

$$L = e^{\overline{\delta^2}} = e^{(4\pi\varepsilon/\lambda)^2}. \tag{53}$$

Normally, L will be small for in-band frequencies because the reflector tolerance ε will be small compared to the in-band wavelength λ. Figure 19 shows curves of roughness loss as a function of frequency for various values of ε/λ_0 where λ_0 is the in-band wavelength. It is seen that roughness loss can increase rapidly with increasing frequency because of the exponential dependence of eq (52). The key parameter is the surface tolerance ε which is not normally known, but has been inferred by Ruze [21] for some antennas from the frequency dependence of the antenna gain. Typical values of ε are on the order of a millimeter or less. For ε = 1 mm and a frequency of 3 GHz (λ_0 = 10 cm), the ratio ε/λ_0 is 0.01, and the center curve in figure 19 would apply. Thus the roughness loss would be negligible at 3 GHz, but would be approximately 7 dB at 30 GHz.

For large values of ε/λ, the second term in eq (50) becomes dominant, and a very broad pattern results. This term depends on a number of parameters including the correlation distance of the surface roughness [21] and will not be considered here. However, it is worth noting that this scatter term can actually raise the pattern level in the distant sidelobes. Strictly speaking, the derivations of Ruze [21] apply to the in-band case, but his results should also apply to the effective aperture at out-of-band frequencies because both cases are described by physical optics integrals.

4.4 Offset Parabolas and Dual Reflectors

The analysis in Sections 2 and 3 was done for a symmetrical paraboloid with a prime focus feed, but other reflector antenna configurations are also of interest. In general, other configurations are more complicated to analyze rigorously, but in many cases can be described by an equivalent symmetrical paraboloid.

Consider first the offset paraboloid shown in figure 20. The offset geometry has the advantage of eliminating blockage by the feed horn. The focal region fields of this geometry have been analyzed by Bem [12] for on-axis incidence ($\theta_s = 0$) and by Valentino and Toulios [11] for arbitrary incidence. Typically, the focal region fields of the offset paraboloid are approximately equal to those of the symnmetrical paraboloid if the equivalent focal length f' and equivalent diameter D' are used in place of f and D. Thus the formulas in Sections 2 and 3 are directly applicable to the offset paraboloid if the equivalent parameters are used. For an offset angle θ_0, the equivalent focal length is given by [12]

$$f' = \frac{2f}{1 + \cos\theta_0}. \tag{54}$$

The equivalent diameter D' is simply the projected diameter in the plane perpendicular to the axis of the parabola as shown in figure 20. The equivalent parameter method is most accurate for small values of θ_0, but Bem [12] has found good results for θ_0 as large as 45°. Also, Valentino and Toulios [11] have shown that the geometrical optics shift as predicted by eq (17) holds for incidence angles of $\theta_s = 5°$ and 10° for an offset parabola with $\theta_s = 44°$.

Symmetrical dual reflector antennas can also be analyzed by replacing them with single reflectors of equivalent focal length as shown by Hannan [24]. Consider the Cassegrain antenna in figure 21. The main reflector is a paraboloid of diameter D and focal length f, and the subreflector is a hyperboloid. The real focal point is shown between the reflectors, and the equivalent single paraboloid (dashed) has a focal length f' and a diameter D. The equivalent focal length can be written as [24]

$$f' = f\,\frac{\tan(\theta_m/2)}{\tan(\theta_m'/2)}. \tag{55}$$

For a Gregorian antenna, the subreflector is a concave ellipse as shown in figure 22. The equivalent paraboloid [24] again has a diameter D and a focal length f' given by eq (55).

Dual reflector antennas have been analyzed by using physical optics on both the main reflector and the subreflector [25]. It was found that the equivalent paraboloid approach worked well for both Cassegrain and Gregorian antennas.

4.5 Coax-to-Waveguide Adapter

In this section we analyze the out-of-band response of a typical coax-to-waveguide adapter. A knowledge of this response is helpful in evaluating the comparison between the reflector antenna theory and the experimental results in Section 3.3. Such adapters are also used in many other microwave antennas which use waveguide feeds, and the adapter response is an important part of the total antenna system response.

The probe type of adapter which we consider is shown in figure 23. Collin [26] has analyzed this structure using a variational technique, and he has presented some numerical results for in-band frequencies where the waveguide supports only a single propagating mode. Here we follow Collin's notation and formulation, but we avoid some of his approximations which were intended only for in-band frequencies.

The main task is to compute the input impedance Z_{in} of the probe as seen by the coaxial cable at the junction (y = 0). Collin [26] has derived the following double integral expression for Z_{in}:

$$Z_{in} = -\frac{1}{I_t^2} \iint_S \iint_S \underline{J}\,(\underline{r}) \cdot \underline{\underline{G}}\,(\underline{r}|\underline{r}') \cdot \underline{J}\,(\underline{r}')\, da\, da', \tag{56}$$

where S is the probe surface, $\underline{J}$ is the surface current on the probe, $\underline{\underline{G}}$ is a dyadic Green's function for the waveguide, and I_t is the total probe current at the junction. Collin has shown that eq (56) is a variational expression for Z_{in}; thus a first-order approximation to $\underline{J}$ yields a second-order approximation to Z_{in}. Consequently, a sinusoidal approximation to the probe current is adequate, and $\underline{J}$ can be written [26]

$$\underline{J} = \underline{a}_y\, J_0 \sin k\,(d - y), \tag{57}$$

where $\underline{a}_y$ is a y-directed unit vector and J_0 is an arbitrary constant. We assume that the current distribution is uniform in the circumferential direction and that I_t is thus given by

$$I_t = \pi\, t\, J_0 \sin kd, \tag{58}$$

where t is the probe diameter.

In evaluating eq (56), it is convenient to write Z_{in} as a mode sum because $\underline{\underline{G}}$ is a mode sum.

$$Z_{in} = \sum_{n=1,3,5}^{\infty} \sum_{m=0}^{\infty} Z_{nm}, \tag{59}$$

where $Z_{nm} = R_{nm} + j\, X_{nm}$.

R_{nm} is the resistance associated with the nm waveguide mode, and X_{nm} is the reactance associated with the nm waveguide mode. The probe excites only TM^y_{nm} modes that are transverse magnetic to y. The fields of the TM^y_{nm} mode have n half cycles in the x direction and m half cycles in the y direction. The terms for n even do not contribute to Z_{in} because the probe is located at the center of the waveguide (x = a/2). For propagating modes, the propagation constant β_{nm} is given by

$$\beta_{nm} = j \sqrt{k^2 - (n\pi/a)^2 - (m\pi/b)^2}, \tag{60}$$

where a and b are the waveguide dimensions indicated in figure 23. For evanescent modes, the attenuation constant Γ_{nm} is given by

$$\Gamma_{nm} = \sqrt{(n\pi/a)^2 + (m\pi/b)^2 - k^2}. \tag{61}$$

Only the propagating modes contribute to the resistive (real) part of Z_{in}, and Collin treated the in-band case where only the TM^y_{10} mode was propagating. If we apply his method of evaluation to an arbitrary nm propagating mode, we obtain the following:

$$R_{nm} = \frac{2\,C_m}{\beta_{nm}} \sin^2 \beta_{nm}\ell,$$
$$X_{nm} = \frac{C_m}{\beta_{nm}} \sin (2\beta_{nm}\ell), \tag{62}$$

where $C_m = \dfrac{\eta\,\varepsilon_{om}}{k\,ab\,\sin^2 kd} \dfrac{[\cos kd - \cos (\frac{m\pi d}{b})]^2}{1 - (\frac{m\pi}{kb})^2}$

and $\varepsilon_{om} = \begin{cases} 1, & m = 0 \\ 2, & m \neq 0 \end{cases}$.

The result in eq (62) agrees with Collin's result for the special case, $n = 1$ and $m = 0$.

The evanescent modes contribute only to the reactance X_{in}. For sufficiently large values of m, we follow the Poisson summation formula of Collin and obtain the following:

$$\sum_{n=1,3,\cdots}^{\infty} X_{nm} \approx \frac{a\,C_m}{2\pi} K_o\,(k_m\,t/2), \tag{63}$$

where $k_m = \sqrt{(m\pi/b)^2 - k^2}$,
and K_o is a zero-order, modified Bessel function [14]. The result in eq (63) is valid for $m \geqslant M$ where $k_M\,a >> 1$. The sum on m from M to ∞ converges rapidly because K_o decays exponentially for large argument [14]. For $m < M$, we perform the n summation using the same asymptotic technique that Collin used for $m = 0$. The technique is based on the following asymptotic behavior of Γ_{nm}^{-1} for large n:

$$\lim_{n\to\infty} \Gamma_{nm}^{-1} \sim \frac{a}{n\pi} - \tfrac{1}{2} \left(\frac{a}{n\pi} \right)^2 \left[\left(\frac{m\pi}{b} \right)^2 - k^2 \right]. \tag{64}$$

However, we must include a term, $\exp(-\Gamma_{nm}\ell)$, which Collin dropped because it was exponentially small for in-band frequencies. When this is done, the sum for $m < M$ is given by

$$\sum_{n=1,2,\cdots}^{\infty}{}' \sum_{m=0}^{M-1}{}' X_{nm} \approx \sum_{m=0}^{M-1} \frac{a\,C_m}{2\pi} \ln \left(\frac{4a}{\pi t} \right)$$
$$+ \sum_{n=1,3,\cdots}^{\infty}{}' \sum_{m=0}^{M-1}{}' C_m \left[\frac{1 - \exp(-2\,\Gamma_{nm}\ell)}{\Gamma_{nm}} - \frac{a}{n\pi} \right] - \sum_{n}^{P} \sum_{m}^{P} C_m \frac{a}{n\pi}. \tag{65}$$

The primes on the summations indicate the omission of the propagating modes that are computed by eq (62) and the P's on the final sum indicate only the propagating modes. The terms in the infinite double sum go to zero as n^{-3} for large n because of the asymptotic behavior of Γ_{nm}^{-1} as given by eq (63).

A computer code for Z_{in} has been written and the double summation over n and m is performed as indicated in figure 24. The boundaries between the three regions depend on the parameters a, b, and k, but the computer code determines the appropriate boundaries automatically. The computer code is fast because both the n summation in eq (65) and the M summation in eq (63) converge rapidly. The code has been checked against Collin's curves for X_{in} and R_{in}, and agreement has been obtained to graphical accuracy.

We now consider the transmission of power from the coaxial cable to the waveguide. We assume that the coaxial cable supports only a dominant TEM mode and that the coaxial cable has a real characteristic impedance R_c. Then the voltage reflection coefficient Γ_v is given by

$$\Gamma_v = \frac{Z_{in} - R_c}{Z_{in} + R_c}. \tag{66}$$

The power reflection coefficient is then given by $|\Gamma_v|^2$, and the transmission coefficient for the total power supplied to the waveguide T_t is

$$T_t = 1 - |\Gamma_v|^2 = \frac{4 R_{in} R_c}{(R_{in} + R_c)^2 + X_{in}^2}. \tag{67}$$

We can also define the transmission coefficient for the nm mode T_{nm} as the ratio of the power transmitted to the nm mode to the incident power in the coaxial cable. By using the relationship between base current I_t and R_{nm} [26], T_{nm} is found to be

$$T_{nm} = \frac{4 R_{nm} R_c}{(R_{in} + R_c)^2 + X_{in}^2}. \tag{68}$$

From eqs (67) and (68), it is easy to see that the total power transmitted to the waveguide is equal to the sum of the power transmitted to the individual propagating modes:

$$T_t = \sum_n \sum_m T_{nm}. \tag{69}$$

In the receiving antenna problem, we are interested in the reciprocal problem where a propagating waveguide mode transmits power to the coaxial cable. By reciprocity, it can be shown that the power transmission coefficient T_{nm} as given by eq (68) also applies to this case.

A computer code was written to compute T_{nm} from eq (68), and it was applied to an S-band coax-to-waveguide adapter. The adapter parameters were chosen to match those used in the reflector antenna which was studied experimentally by Cown, et al. [5,27]: a = 7.112 cm, b = 3.302 cm, d = 1.9 cm, and ℓ = 2.4 cm. The radius of the probe was not given, but we assumed a value of t/2 = 3.5 mm in order to yield a small reactance at 3 GHz. The assumed value of t is not critical because the results are only weakly dependent on the probe radius. The transmission coefficients as a function of frequency are shown in figures 25 and 26. Note that the transmission coefficient for the dominant TM^y_{10} mode is nearly unity from about 2.5 to 5.0 GHz. Above 5 GHz, higher order modes begin to appear, and the results are very frequency sensitive. Some related calculations have been done by Cown and Ryan [27], but they did not compute the reactance of the probe which is required to compute transmission coefficients as indicated by eq (68). At 10 GHz, there are five propagating modes (TM^y_{10}, TM^y_{11}, TM^y_{30}, TM^y_{31}, and TM^y_{12}) which are coupled to the adapter. In addition, there are propagating TE^y_{nm} (transverse electric) and propagating TM^y_{nm} modes with n even [27], but these modes do not couple to the adapter. All of the transmission coefficients have a null at 7.9 GHz because the sinusoidal current assumption in eq (57) yields an infinite value of Z_{in} at kd = π.

In the earlier comparison between theory and experiment for on-axis gain in figure 14, the experimental values were well below the theoretical results. The main problem with the comparison was that the theory included only the antenna response while the experiment included the antenna plus the adapter response [27]. No attempt was made to separate the antenna and adapter responses because the out-of-band response of the adapter was not known. Even though we now have theoretical results for the adapter response, it is not clear how to combine the results with the reflector antenna theory at out-of-band frequencies where higher order modes are propagating in the waveguide. If we take the total transmission coefficient T_t as given by eqs (67) or (69) and multiply by the effective aperture of the antenna, then a corrected frequency response is obtained as shown in figure 27. The correction can be made in other ways, but no precise correction can be made because the antenna theory gives only the total waveguide power, not the modal content. However, the adapter correction does improve the agreement significantly, particularly below 7.5 GHz. The null in the adapter response at 7.9 GHz is not apparent in the experimental data, but no measurements were made between 7.5 and 8.0 GHz. Above 8 GHz, the agreement is not as good, but this is probably because the adapter theory is less accurate when the probe is longer than a half wavelength.

It might be possible to improve the adapter theory for higher frequencies ($kd > \pi$) by using a more accurate distribution for the probe current [26], but it is doubtful that the detailed structure above 8 GHz in figure 27 could be obtained. The thin wire and small coaxial gap assumptions are not really valid above 8 GHz, and also the constructive and destructive interference of the higher order waveguide modes is probably responsible for the rapid frequency variations in figure 27. The main point of figure 27 is that the theory matches the experimental results fairly well in the region where the adapter theory is valid (below 7.5 GHz), and we can expect the reflector antenna theory to remain valid for higher frequencies because it is a high frequency theory. It might be desirable to study the isolated adapter response experimentally, but it might be difficult to perform a meaningful experiment because of the higher order modes.

5. Conclusions

The response of reflector antennas to out-of-band (above-band) frequencies has been studied in a two-step analysis. In Section 2, the electric and magnetic fields and the Poynting vector in the focal region of a paraboloidal reflector have been determined by a physical optics integration. The large f/D approximation is found to be sufficiently accurate for most realistic antennas (f/D > 0.3), and numerical integration is therefore not required. The second step of the analysis is an integration of the Poynting vector over the aperture of the feed horn to obtain the received power. As shown in

Section 3, this integration can also be done by an analytical approximation in order to eliminate the need for numerical integration. The results yield a generalized effective aperture (the total received power divided by the incident power density) for the antenna, and a fairly simple expression gives both the frequency response and the receiving pattern.

The theoretical results have been compared with published measured results for a symmetrical paraboloid with f/D = 0.32 over a frequency range from 3 GHz (in-band) to 10 GHz. The theoretical pattern shape matches the envelope of the measured pattern, but the measured gain falls well below the theoretical result. When the transmission characteristics of the coax-to-waveguide adapter are taken into account, the agreement between theory and experiment is much better. Two important results of the theory are that the beamwidth at out-of-band frequencies is approximately the same as the in-band beamwidth and that there are no high sidelobes. These results are in agreement with the published measured data [27].

In Section 4, a number of extensions to the basic physical optics model are discussed. The level of the distant sidelobes is examined using GTD and is found to be in approximate agreement with physical optics. The transient fields in the focal region are examined for pulse excitation, and the pulse stretching is in agreement with simple geometrical arguments. The effect of reflector roughness is examined, and the reduction in gain or effective aperture can be calculated if the surface tolerance is known. Extensions of the theory for a symmetrical reflector to the cases of offset or dual reflectors is accomplished by using equivalent focal length and diameter. Also, the previous theory for the response of a coax-to-waveguide adapter is extended from the in-band case [26] to the out-of-band case. This theory might be useful for other microwave antennas using the same type of adapter in the feed system.

Other extensions and improvements to the model, such as a more precise treatment of the feed horn, are certainly possible, but the physical optics model presented here is probably adequate for typical out-of-band applications. The analysis of other common microwave antenna types, such as phased arrays, is recommended as having highest priority.

The Defense Nuclear Agency (DNA) supported the research described in this report. The author is grateful to the technical staff of the National Bureau of Standards for numerous technical discussions during the course of this work. Many thanks also go to Captain David Stone of DNA for his continuous interest and support.

6. References

[1] Lind, W.R. Out of band performance of antennas. Moore School of Electrical Engineering Report No. 65-18; 1965.

[2] Levinson, D.S. Transmission-line measurement techniques. Rome Air Development Center Technical Report No. RADC-TR-65-187; 1965.

[3] Cown, B.J.; Cain, F.L.; Duffy, E.G. Statistical prediction model for EMC analysis of out-of-band phased array antennas. IEEE Trans. Electromag. Compat., EMC-18: 163-170; 1976.

[4] Wells, T.C.; Ryan, E.C. Out-of-band reflector antenna model. Georgia Institute of Technology, Engineering Experiment Station, Contract No. DAAG29-80-C-0083; 1981.

[5] Cown, B.J.; Ryan, E.C.; Weaver, E.E. Antenna pattern measurements to characterize the out-of-band behavior of reflector antennas. Georgia Institute of Technology, Engineering Experiment Station, Report ECAC-TR-83-003; 1983.

[6] Kennaugh, E.M.; Ott, R.H. Fields in the focal region of a parabolic receiving antenna. IEEE Trans. Ant. Propagat., AP-12: 376-377; 1964.

[7] Minnett, H.C.; Thomas, B.M. A method of synthesizing radiation patterns with axial symmetry. IEEE Trans. Ant. Propagat. AP-14: 654-656; 1966.

[8] Minnett, H.C.; Thomas, B.M. Fields in the image space of symmetrical focusing reflectors. Proc. IEE, 115: 1419-1430; 1968.

[9] Thomas, B.M. Matching focal region fields with hybrid modes. IEEE Trans. Ant. Propagat. AP-18: 404-405; 1970.

[10] Landry, M.; Chasse, Y. Measurement of electromagnetic intensity in focal region of wide-angle paraboloid reflector. IEEE Trans. Ant. Propagat., AP-19: 539-43; 1971.

[11] Valentino, A.R.; Toulios, P.P. Fields in the focal region of offset parabolic antennas. IEEE Trans. Ant. Propagat., AP-24: 859-865; 1976.

[12] Bem, D.J. Electric-field distribution in the focal region of an offset paraboloid. Proc. IEE, 116: 679-684; 1969.

[13] Kraus, J.D. Antennas. New York: McGraw Hill; 1950.

[14] Abramowitz, M.; Stegun, I.A., ed. Handbook of mathematical functions. Nat. Bur. Stand. (U.S.) Handb. AMS 55; 1964.

[15] Stubenrauch, C.F.; Yaghjian, A.D. Determination of mutual coupling between co-sited microwave antennas and calculation of near-zone electric field. Nat. Bur. Stand. (U.S.) Interagency Report 80-1630; 1981.

[16] James, G.L. Geometrical theory of diffraction for electromagnetic waves. Stevenage: Peter Peregrinus; 1976.

[17] CCIR, International Radio Consultative Committee. Documents of the XIVth Plenary Assembly. Geneva; 1978.

[18] Roberts, E.C.; Kaufman, H. Table of Laplace transforms. Philadelphia: W.B. Saunders Co.; 1966, p. 297.

[19] Papoulis, A. The Fourier integral and its applications. New York: McGraw-Hill; 1962, p. 274.

[20] Morse, P.M.; Feshbach, H. Methods of theoretical physics. New York: McGraw-Hill; 1953, Sec. 11.3.

[21] Ruze, J. Antenna tolerance theory - a review. Proc. IEEE, 54: 633-640; 1966.

[22] Rahmat-Samii, Y. An efficient computational method for characterizing the effects of random surface errors on the average power pattern of reflectors. IEEE Trans. Ant. Propagat., AP-31: 92-98, 1983.

[23] Tripp, V.K. A new approach to the analysis of random errors in aperture antennas. IEEE Trans. Ant. Propagat., AP-32: 857-863; 1984.

[24] Hannan, P.W. Microwave antennas derived from the Cassegrain telescope. IEEE Trans. Ant. Propagat., AP-9: 140-153, 1961.

[25] Doan, D.L.; Vu, T.B. Focal region fields of dual reflector antennas. IEEE Trans. Ant. Propagat., AP-25: 392-396; 1977.

[26] Collin, R.E. Field theory of guided waves. New York: McGraw-Hill; 1960, Sec. 7.1.

[27] Cown, B.J.; Ryan, C.E. Near-field theory and techniques for wideband radiating systems at in-band and out-of-band frequencies. Georgia Institute of Technology, Engineering Experiment Station, Contract No. DAAG29-78-C-0029; 1982.

[28] Wheelan, A.D. Tables of summable series and integrals involving Bessel functions. San Francisco: Holden-Day; 1968, p. 8.

Appendix A
Evaluation of the ϕ_1 Integration

The first step in the evaluation of eq (6) is to write the phase term in the following form:

$$\Omega_s + R = M_o - M_1 \cos(\phi_1 - \psi), \tag{A1}$$

where M_o, M_1, and ψ are independent of ϕ_1. From eqs (7) and (8), we find that the three quantities are given by

$$M_o = A_o + r_1,$$
$$M_1 = \sqrt{(A_c + B_c)^2 + B_s^2}, \tag{A2}$$

$$\text{and } \psi = \sin^{-1} (B_s/M_1),$$

$$\text{where } A_o = (f - r_1) \cos\theta_s,$$

$$A_c = r_1 \sin\theta_1 \sin\theta_s,$$

$$B_c = - r_2 \sin\theta_1 \cos\phi_2$$

$$\text{and } B_s = - r_2 \sin\theta_1 \sin\phi_2.$$

The next step is to express the amplitude terms in eq (6) in terms of a Fourier series in ϕ_1. When this is done, it is found that the series truncates at n = 2, and $d\underline{E}$ and $d\underline{H}$ can be written:

$$d\underline{E} = - j \frac{E_i f}{\lambda} e^{-jk (M_o + M_1 \cos\psi)}.$$

$$\{ \sum_{n=0}^{2} [C_{xn}\cos n\phi_1 + S_{xn}\sin n\phi_1) \underline{u}_x + \sum_{n=0}^{2} [C_{yn}\cos n\phi_1 + S_{yn}\sin n\phi_1] \underline{u}_y$$

$$+ \sum_{n=0}^{2} [C_{zn}\cos n\phi_1 + S_{zn}\sin n \phi_1) \underline{u}_z\} \frac{2 \sin\theta_1}{1 + \cos\theta_1} d\theta, d\phi,$$

and (A3)

$$d\underline{H} = - j \frac{E_i f}{\lambda} e^{-jk} (M_o + M_1 \cos\psi) .$$

$$\{ \sum_{n=0}^{2} [D_{xn}\cos n\phi_1 + F_{xn}\sin n\phi_1] \underline{u}_x + \sum_{n=0}^{2} [D_{yn}\cos n\phi_1 + F_{yn}\sin n\phi_1] \underline{u}_y$$

$$+ \sum_{n=0}^{2} [D_{zn}\cos n\phi_1 + F_{zn}\sin n\phi_1] \underline{u}_z \} \frac{2 \sin\theta_1}{1 + \cos\theta_1} d\theta, d\phi_1 .$$

The Fourier coefficients are obtained from the terms inside the brackets in eq (6) and found to be:

$$C_{x0} = a_y \left(\cos\theta_1 + \tfrac{1}{2} \frac{\sin^2\theta_1}{1 + \cos\theta_1}\right), \quad S_{x0} = 0,$$

$$C_{x1} = 0 \quad , \quad S_{x1} = - a_z \frac{\sin\theta_1}{1 + \cos\theta_1} ,$$

$$C_{x2} = - \tfrac{1}{2} a_y \frac{\sin^2\theta_1}{1 + \cos\theta_1} \quad , \quad S_{x2} = \tfrac{1}{2} a_x \frac{\sin^2\theta_1}{1 + \cos\theta_1} ,$$

$$C_{y0} = a_x\left(\cos\theta_1 + \tfrac{1}{2} \frac{\sin^2\theta_1}{1 + \cos\theta_1}\right) \quad , \quad S_{y0} = 0,$$

$$C_{y1} = a_z \frac{\sin\theta_1}{1 + \cos\theta_1} \quad , \quad S_{y1} = 0,$$

$$C_{y2} = - \tfrac{1}{2} a_x \frac{\sin^2\theta_1}{1 + \cos\theta_1} \quad , \quad S_{yz} = - \frac{a_y}{z} \frac{\sin^2\theta_1}{1 + \cos\theta_1} ,$$

$$C_{z0} = 0 \quad , \quad S_{z0} = 0,$$

$$C_{z1} = - a_y \sin\theta_1 \quad , \quad S_{z1} = a_x \sin\theta_1,$$

$$C_{z2} = 0 \quad , \quad S_{z2} = 0,$$

and (A4)

$$D_{x0} = \frac{a_x}{2}(1 + \cos\theta_1) \quad , \quad F_{x0} = 0,$$

$$D_{x1} = -a_z \frac{\cos\theta_1 \sin\theta_1}{1 + \cos\theta_1} \quad , \quad F_{x1} = 0,$$

$$D_{x2} = -\frac{a_x}{2} \frac{\sin^2\theta_1}{1 + \cos\theta_1} \quad , \quad F_{x2} = \frac{-a_y}{2} \frac{\sin^2\theta_1}{1 + \cos\theta_1},$$

$$D_{y0} = \frac{a_y}{2}(1 + \cos\theta_1) \quad , \quad F_{y0} = 0$$

$$D_{y1} = 0 \quad , \quad F_{y1} = -a_z \frac{\sin\theta_1 \cos\theta_1}{1 + \cos\theta_1},$$

$$D_{y2} = \frac{a_y}{2} \frac{\sin^2\theta_1}{1 + \cos\theta_1} \quad , \quad F_{y2} = \frac{a_x}{2}(\cos\theta_1 - 1)$$

$$D_{z0} = a_z \frac{\sin^2\theta_1}{1 + \cos\theta_1} \quad , \quad F_{y0} = 0,$$

$$D_{z1} = -a_x \sin\theta_1 \quad , \quad F_{y1} = -a_y \sin\theta_1,$$

$$D_{z2} = 0 \quad , \quad F_{y2} = 0.$$

From Fourier-Bessel expansions [2.7], we can derive the following useful integral:

$$\int_0^{2\pi} \left\{ \begin{matrix} \cos n\phi \\ \sin n\phi \end{matrix} \right\} e^{-jk M_1 \cos(\phi_1 - \psi)} d\phi_1 = 2\pi j^n \left\{ \begin{matrix} \cos n\psi \\ \sin n\psi \end{matrix} \right\} J_n (k M_1), \qquad \text{(A5)}$$

where J_n is the nth order Bessel function. By using eqs (A5) in (A3), the ϕ_1 integrations can be carried out to yield the desired expressions for $\underline{E}$ and $\underline{H}$ in eq (13).

Open-ended Waveguide

Consider the two-dimensional, open-ended waveguide of width w in figure 28. A plane wave is incident in the xz plane, and the incident electric field is y polarized:

$$E_{yi} = E_o e^{jk\,(z\cos\theta + x\sin\theta)}, \tag{B1}$$

where θ is the incidence angle measured from the z axis. The y component of the incident Poynting vector S_z is given by

$$S_z = -\frac{|E_o|^2}{2\eta}\cos\theta. \tag{B2}$$

From eq (23), the approximate received power per unit length P_r is given by

$$P_r = P_o\cos\theta, \tag{B3}$$

where $P_o = w\,S_o$ and $S_o = \frac{|E_o|^2}{2\eta}$.

If we make the Kirchhoff approximation in the waveguide aperture ($z = 0$, $|x| < w/2$), then the electric field is given by

$$E_y\Big|_{z=0} = E_o e^{jkx\sin\theta} \tag{B4}$$

A general waveguide mode expansion for the electric field E_y is

$$E_y = \sum_{n=1}^{\infty} \left[c_n \cos\frac{(2\,n-1)\,\pi x}{w}\, e^{jk_{xe}z} + s_n \sin\frac{2n\,\pi x}{w}\, e^{jk_{xo}z}\right], \tag{B5}$$

where $k_{xe} = \sqrt{k^2 - \left[\frac{(2\,n-1)\,\pi}{w}\right]^2}$

and $k_{xo} = \sqrt{k^2 - \left(\frac{2n\pi}{w}\right)^2}$.

The cutoff wavelength λ_c is determined by setting $k_{xe} = 0$ for the even (in x) modes and by setting $k_{xo} = 0$ for the odd (in x) modes:

$$\text{Even:}\quad k_{xe} = 0 \qquad \lambda_c = \frac{2w}{2\,n-1}\,,$$
$$\text{Odd:}\quad k_{xo} = 0 \qquad \lambda_c = \frac{w}{n}\,. \tag{B6}$$

The unknown coefficients are determined by matching the electric field at $y = 0$ in eqs (B4) and (B5)

$$E_o\, e^{jkx \sin\theta} = \sum_{n=1}^{\infty} [c_n \cos \frac{(2\,n-1)\,\pi x}{w} + s_n \sin \frac{2n\,\pi x}{w}]. \tag{B7}$$

By using the orthogonality relationships for the cosine and sine functions in eq (B7), we obtain the following expressions for c_n and s_n:

$$c_n = E_o \left\{ \frac{\sin [\frac{kw}{2} \sin\theta + \frac{(2\,n-1)\,\pi}{2}]}{[\frac{kw}{2} \sin\theta + \frac{(2\,n-1)\,\pi}{2}]} + \frac{\sin [\frac{kw}{2} \sin\theta - \frac{(2\,n-1)\,\pi}{2}]}{[\frac{kw}{2} \sin\theta - \frac{(2\,n-1)\,\pi}{2}]} \right\}$$

and (B8)

$$s_n = \frac{E_o}{j} \left\{ \frac{\sin [\frac{kw \sin\theta}{2} + \frac{n\pi}{2}]}{[\frac{kw \sin\theta}{2} + \frac{n\pi}{2}]} - \frac{\sin [\frac{kw \sin\theta}{2} - \frac{n\pi}{2}]}{[\frac{kw \sin\theta}{2} - \frac{n\pi}{2}]} \right\}.$$

The sin ( )/( ) in eq (B8) have peaks where the transverse wave numbers of the even and odd waveguide modes, $(2\,n-1)\pi/w$ and $2n\pi/w$, match the transverse wave number of the incident field, $k \sin\theta$.

In order to compute the power in the waveguide modes, we need an expression for the magnetic field $\underline{H}$:

$$\underline{H} = \frac{j}{\omega\mu} \nabla \times \underline{u}_y\, E_y. \tag{B9}$$

From eq (B9) the magnetic field components H_x and H_z are

$$H_x = \frac{1}{j\omega\mu} \frac{\partial E_y}{\partial z} \text{ and } H_z = \frac{-1}{j\omega\mu} \frac{\partial E_y}{\partial x}. \tag{B10}$$

The power per unit length transmitted by the waveguide P_g is given by

$$P_g = \int_{-w/2}^{w/2} \mathrm{Re}\, (E_y H_z^*)\, dx. \tag{B11}$$

By substituting eqs (B5) and (B10) into (B11) and carrying out the x integration, we obtain

$$P_g = \sum_{n=1}^{\infty} (P_{ne} + P_{no}), \tag{B12}$$

where $P_{ne} = \frac{w}{4k\eta} |c_n|^2 \, \mathrm{Re}\,(k_{xe})$

and $P_{no} = \frac{w}{4k\eta} |s_n|^2 \, \mathrm{Re}\,(k_{xo})$.

For modes above cutoff, k_{xe} and k_{xo} are real. For modes below cutoff, k_{xe} and k_{xo} are purely imaginary. Thus, only the propagating modes carry power, and the summation in eq (B12) can be truncated.

A check on the accuracy of the Kirchhoff approximation for the aperture field in eq (B4) can be made by comparing the waveguide power P_g in eq (B12) with the received power approximation P_r in eq (B3). In general, the evaluation of eq (B12) must be done numerically for specific parameters. However, the limit for large kw can be evaluated analytically for on-axis incidence, $\theta=0$. In this case, the mode coefficients are given by

$$c_n = \frac{4\,(-1)^{n-1}}{(2\,n-1)\,\pi} E_o \text{ and } s_n = 0. \tag{B13}$$

For large kw, $k_{xe} \simeq k$, and P_g is given by

$$P_g = \frac{4w\left|E_o\right|^2}{\pi^2\,\eta} \sum_{n=1}^{\infty} (2\,n-1)^{-2}. \tag{B14}$$

The infinite sum has a known result [28]:

$$\sum_{n=1}^{\infty} (2\,n-1)^{-2} = \frac{\pi^2}{8}. \tag{B15}$$

Substituting eq (B15) into eq (B14), we have

$$P_g = \frac{w\left|E_o\right|^2}{2\eta} = w\,S_o = P_r. \tag{B16}$$

Thus Kirchhoff approximation yields a consistent result for the received power and the waveguide power when kw is very large.

In figures 29-31, we show results for the received power and the waveguide power as a function of θ for various values of w/λ. In all cases, the various powers are normalized to the incident power P_0 at $\theta=0$. As w/λ is increased from 1.5 to 10, the agreement between P_r and P_g improves for all incidence angles. In all cases, the powers in the first even and odd modes are shown for comparison. As w/λ is increased, the mode patterns show more rapid oscillation, and the number of propagating modes increases. For $w/\lambda = 1.5$, there are only 2 propagating modes, but for $w/\lambda = 10$, there are 19 propagating modes.

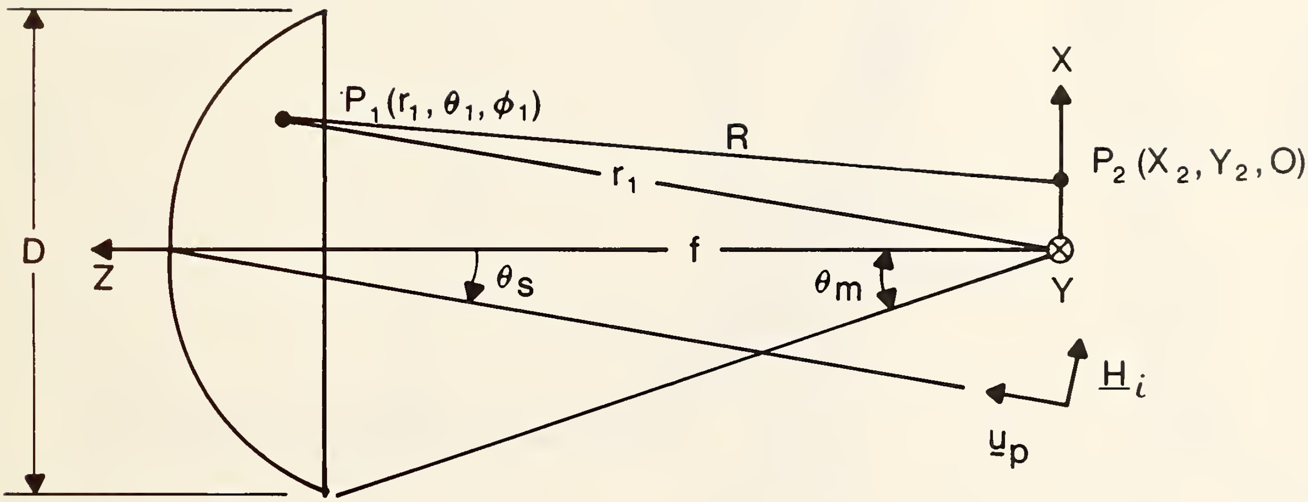

Figure 1. Geometry for a plane wave incident on a symmetrical parabolic reflector.

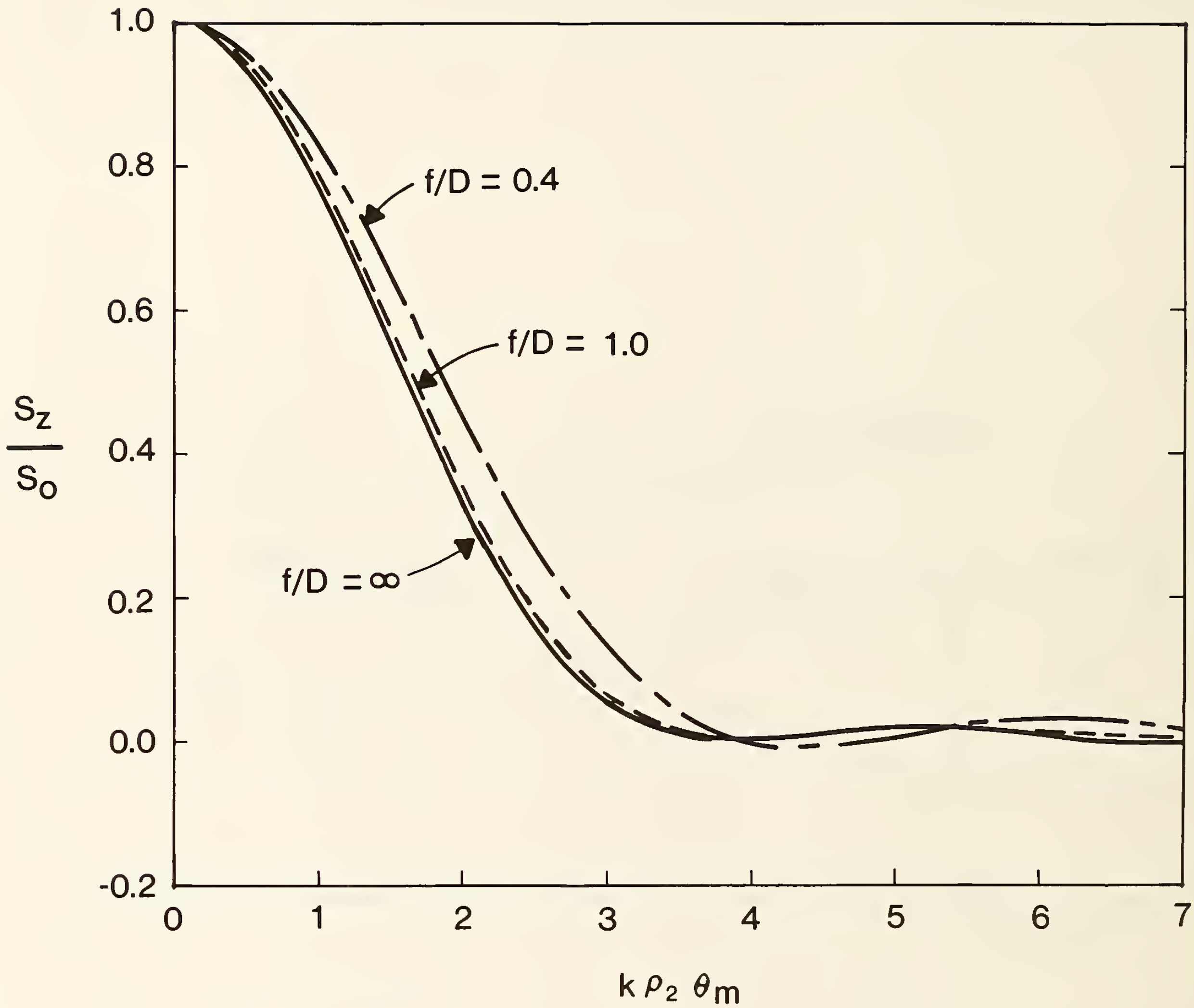

Figure 2. Normalized Poynting vector for on-axis incidence.

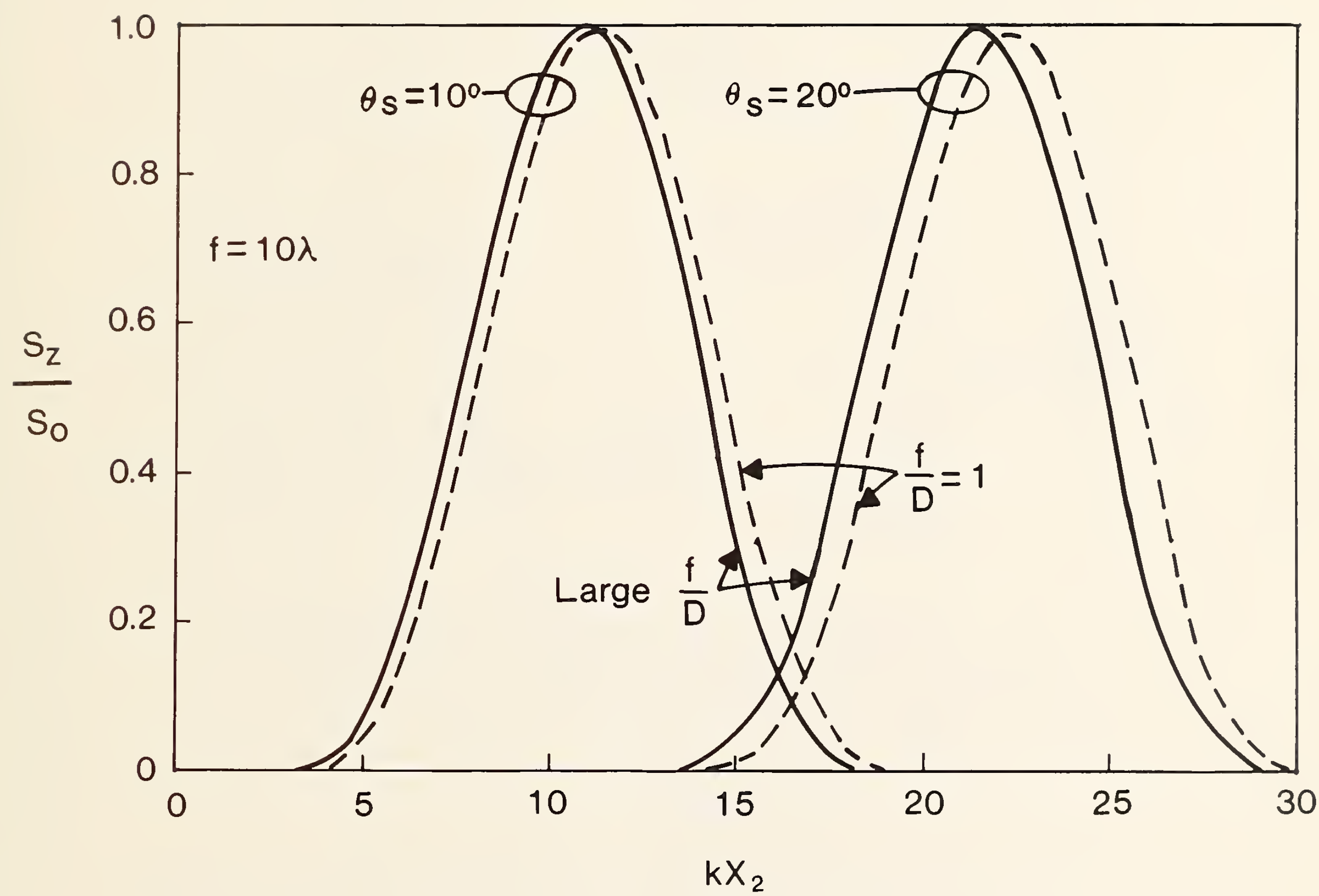

Figure 3. Normalized Poynting vector for off-axis incidence.

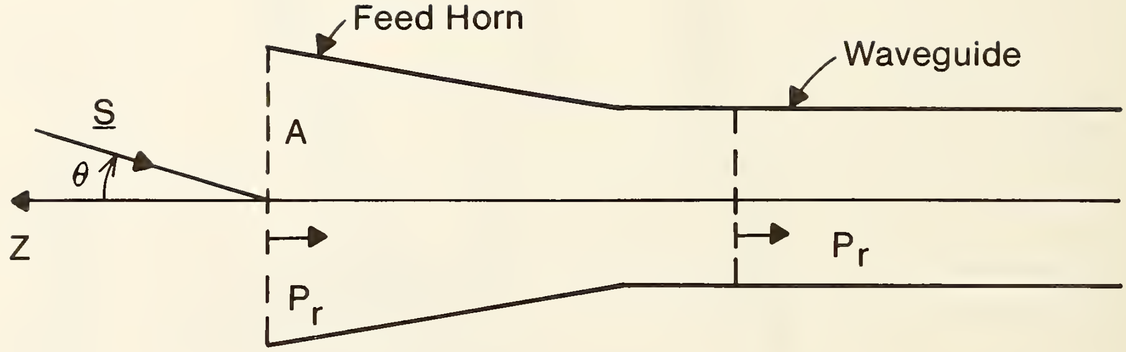

Figure 4. Geometry for a circular feed horn.

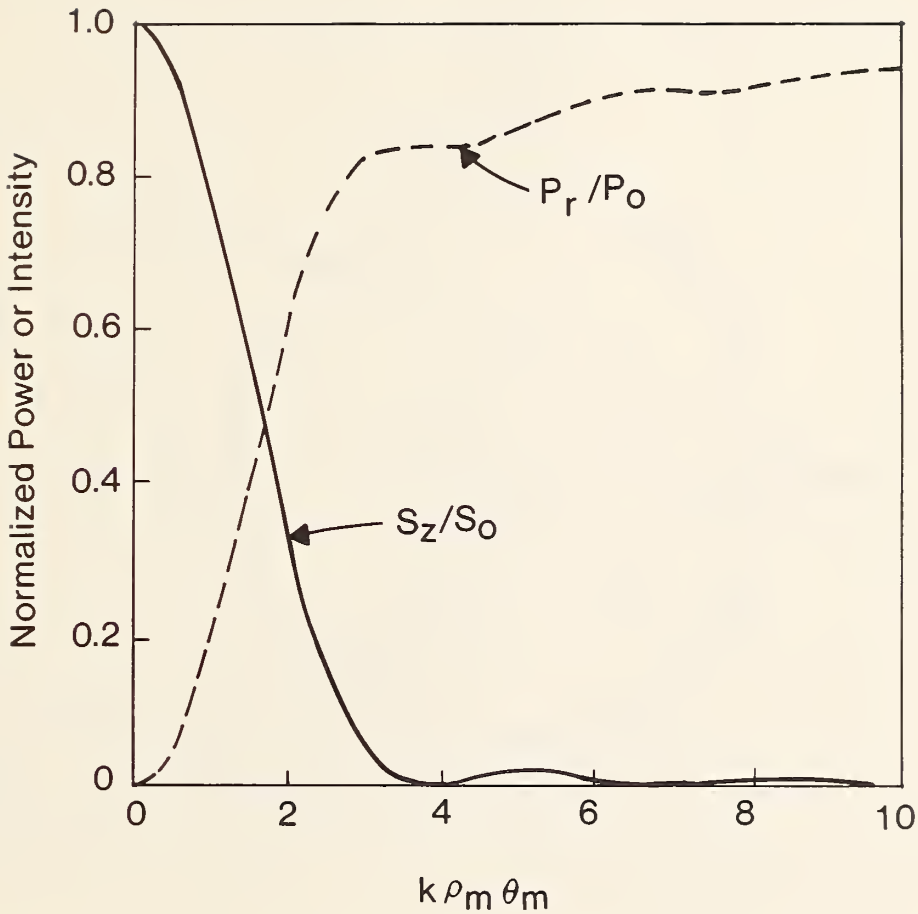

Figure 5. Normalized Poynting vector and received power for on-axis incidence.

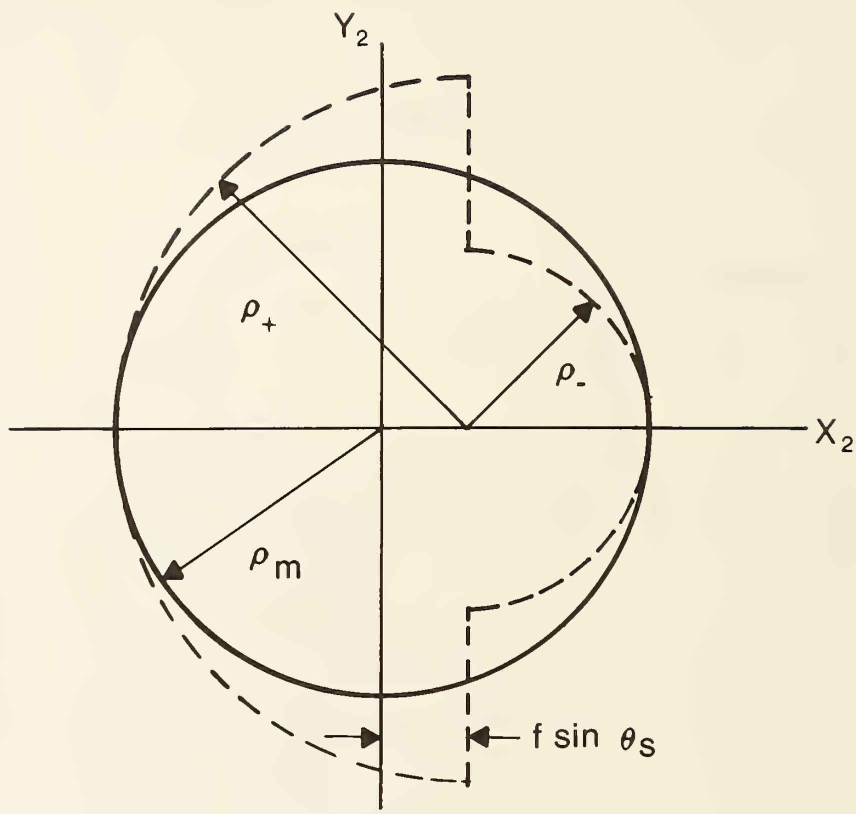

Figure 6. Approximate integration surface (dashed) for off-axis incidence. The geometrical optics point is located inside the circle.

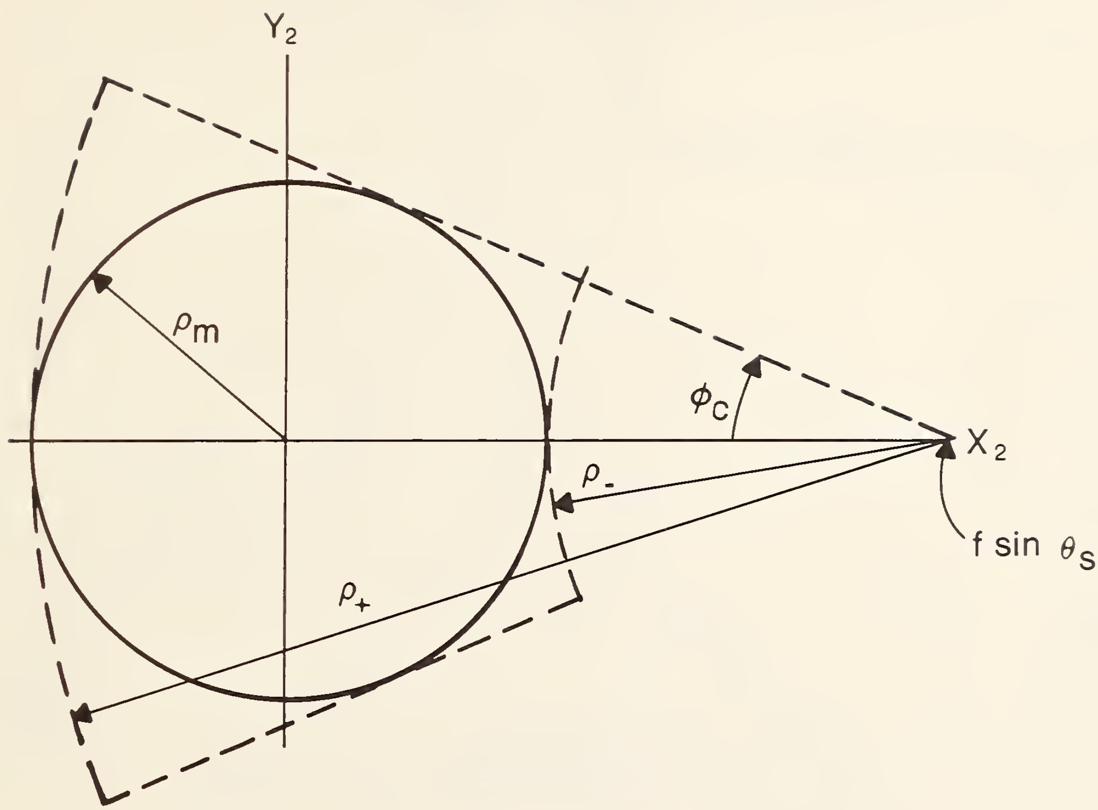

Figure 7. Approximate integration surface (dashed) for off-axis incidence. The geometrical optics point is located outside the circle.

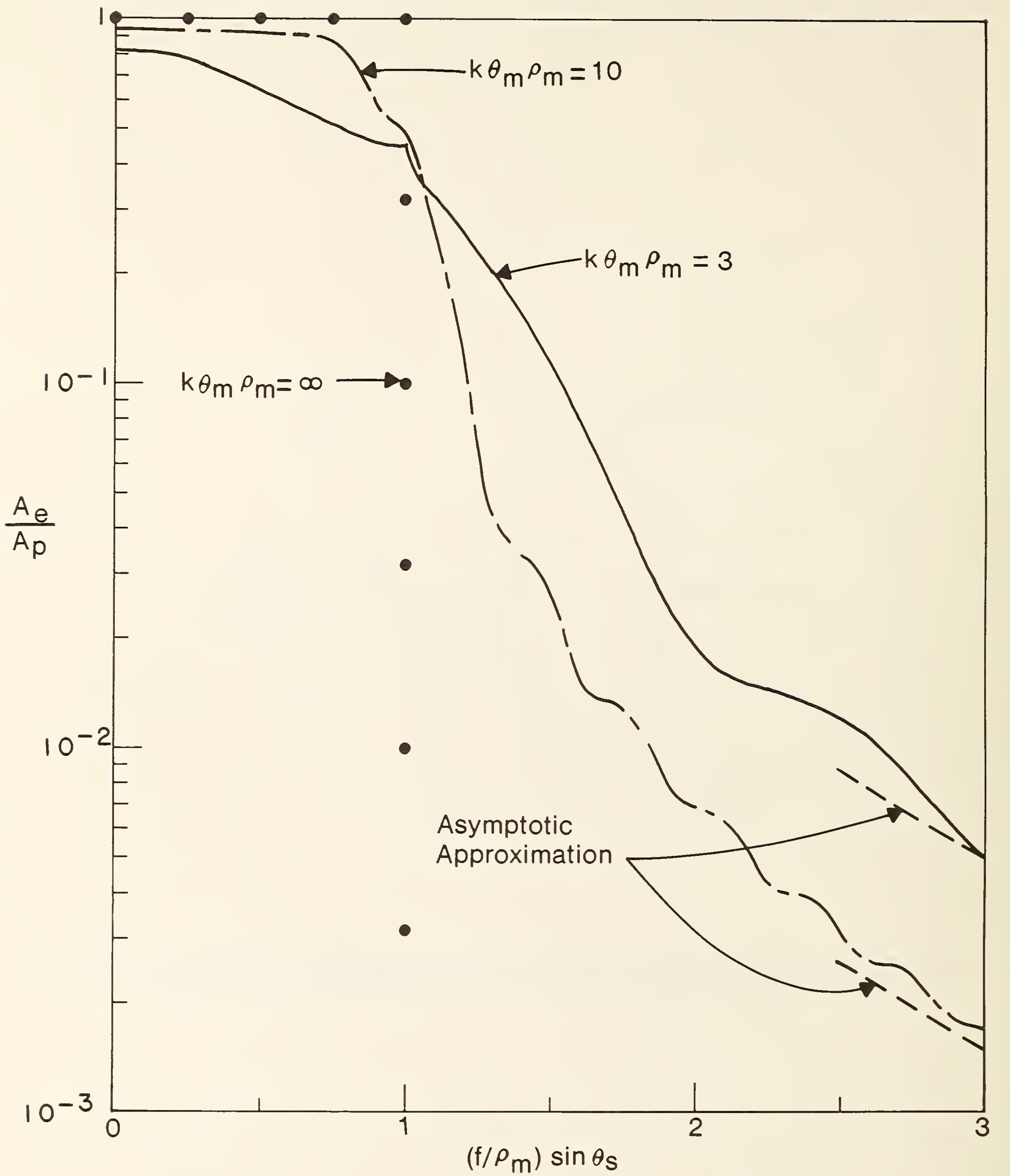

Figure 8. Normalized effective aperture for off-axis incidence.

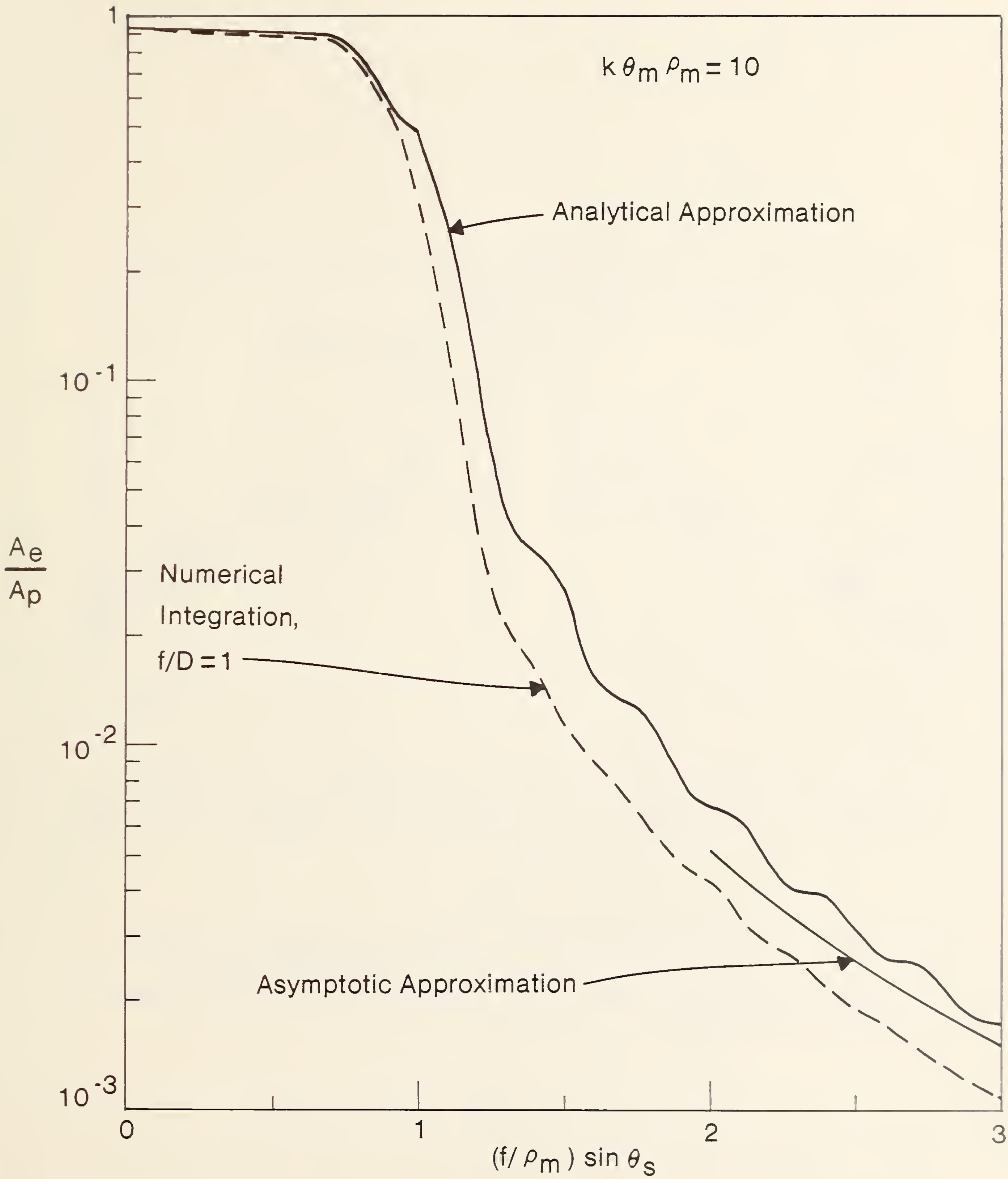

Figure 9. Comparison of analytic and numerical results for the effective aperture.

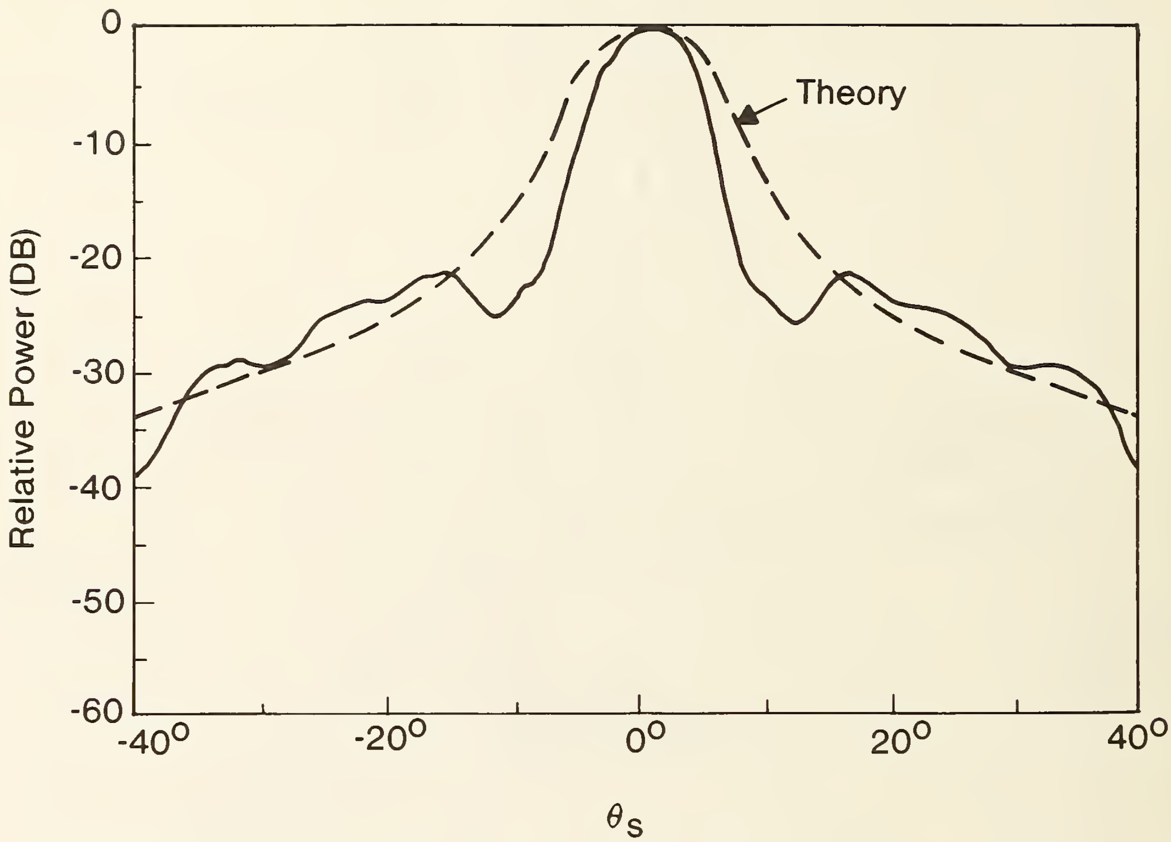

Figure 10. Comparison of theory and experiment [3.3] for the in-band frequency of 3 GHz.

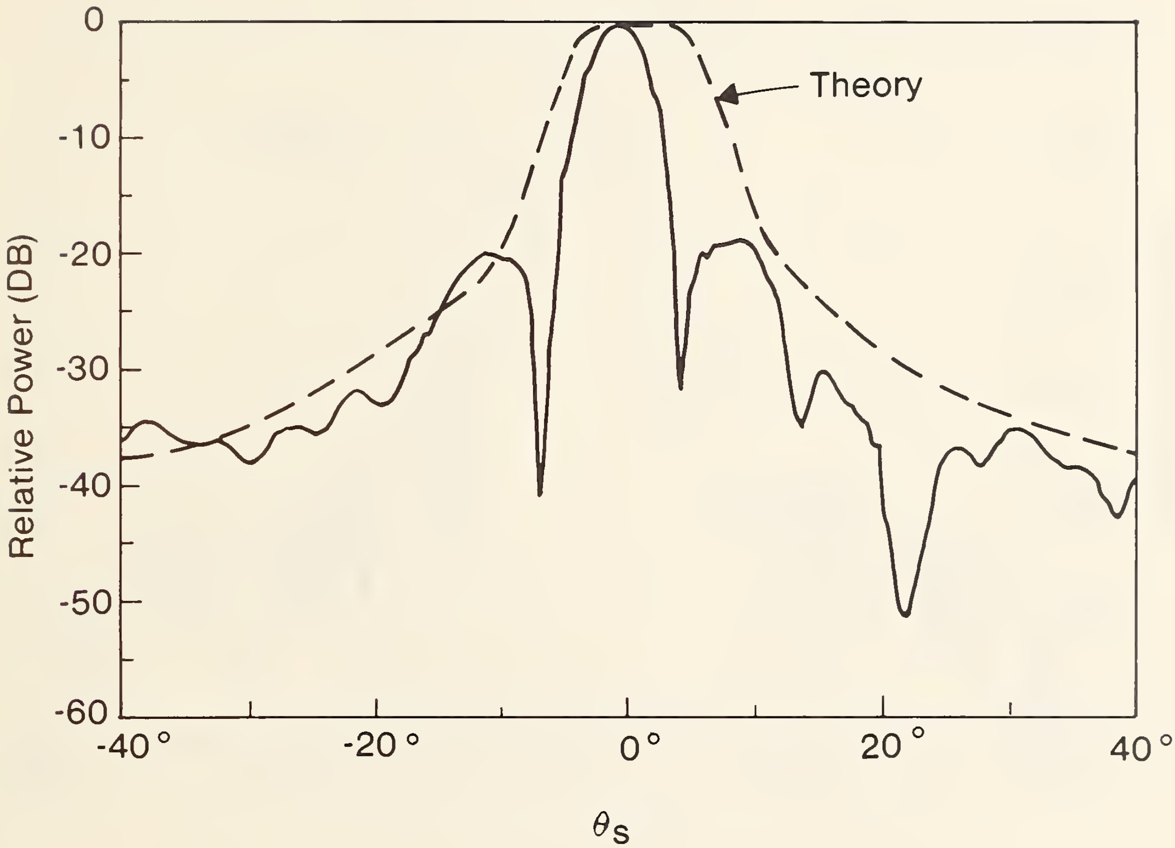

Figure 11. Comparison of theory and experiment [5] for an out-of-band frequency of 6 GHz.

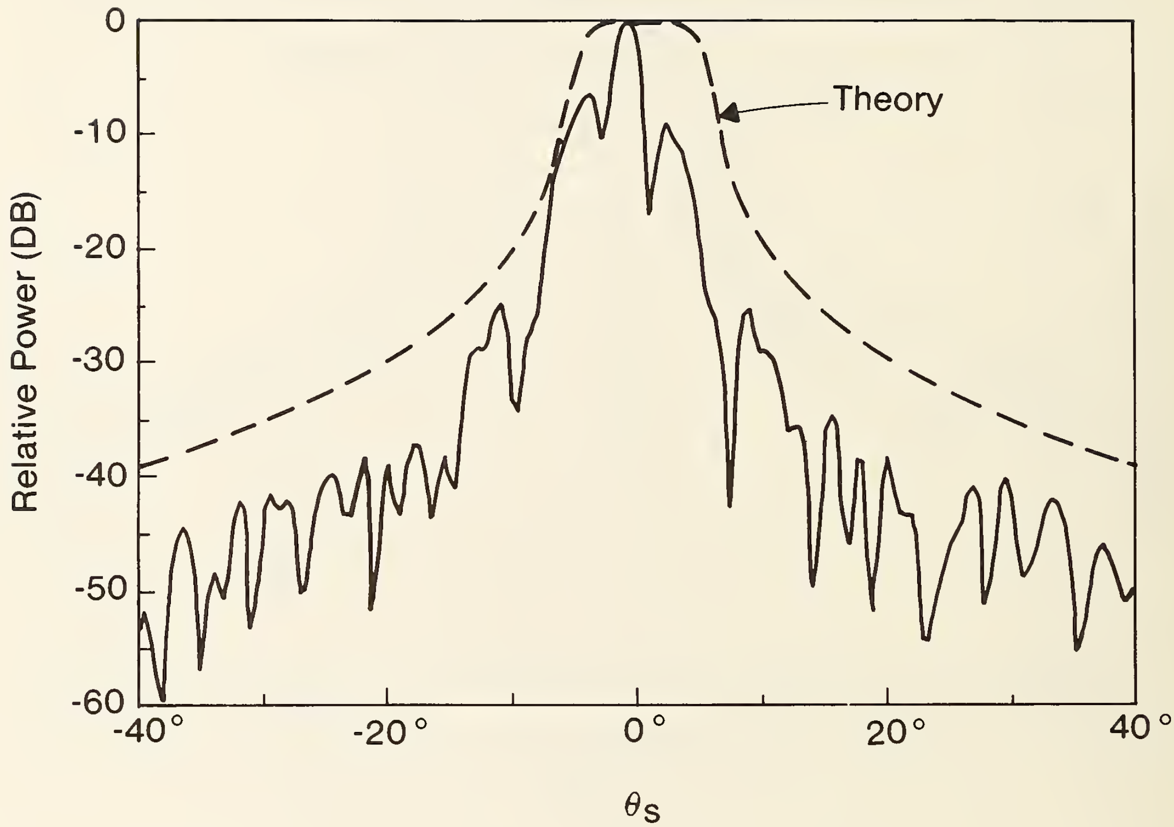

Figure 12. Comparison of theory and experiment [5] for an out-of-band frequency of 8 GHz.

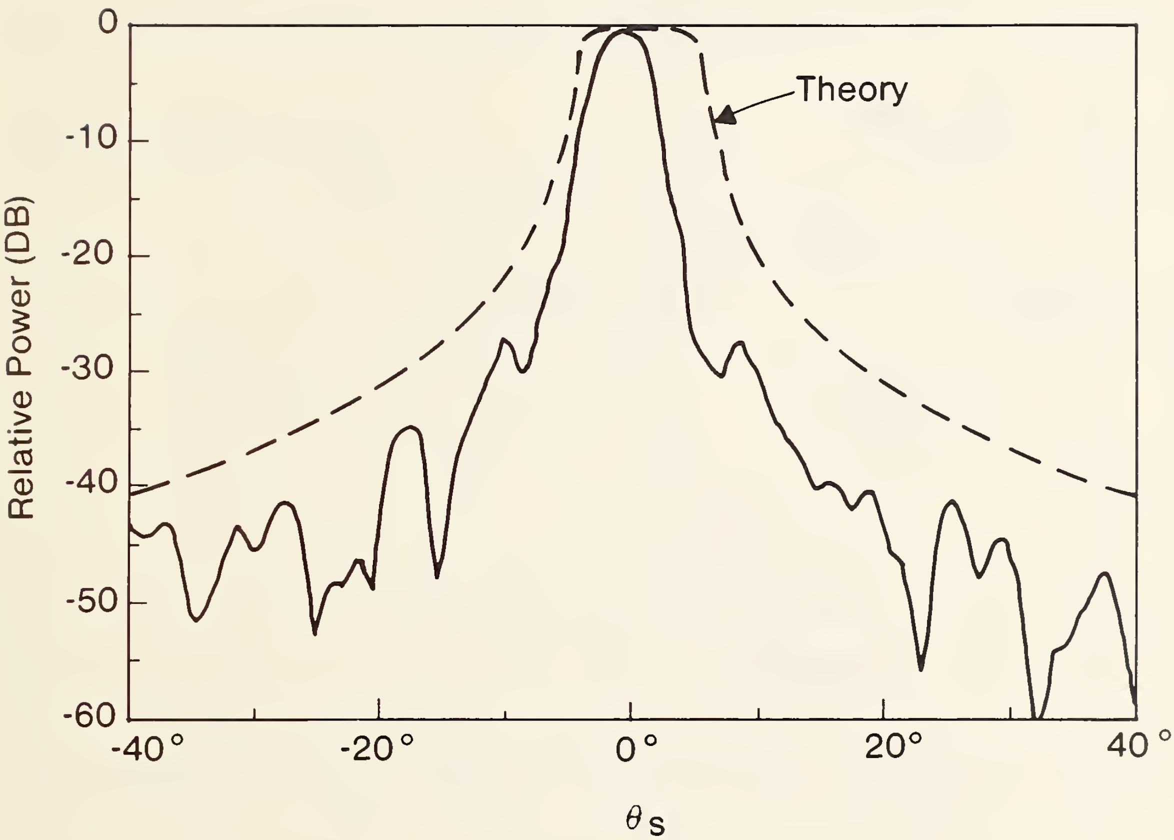

Figure 13. Comparison of theory and experiment [5] for an out-of-band frequency of 10 GHz.

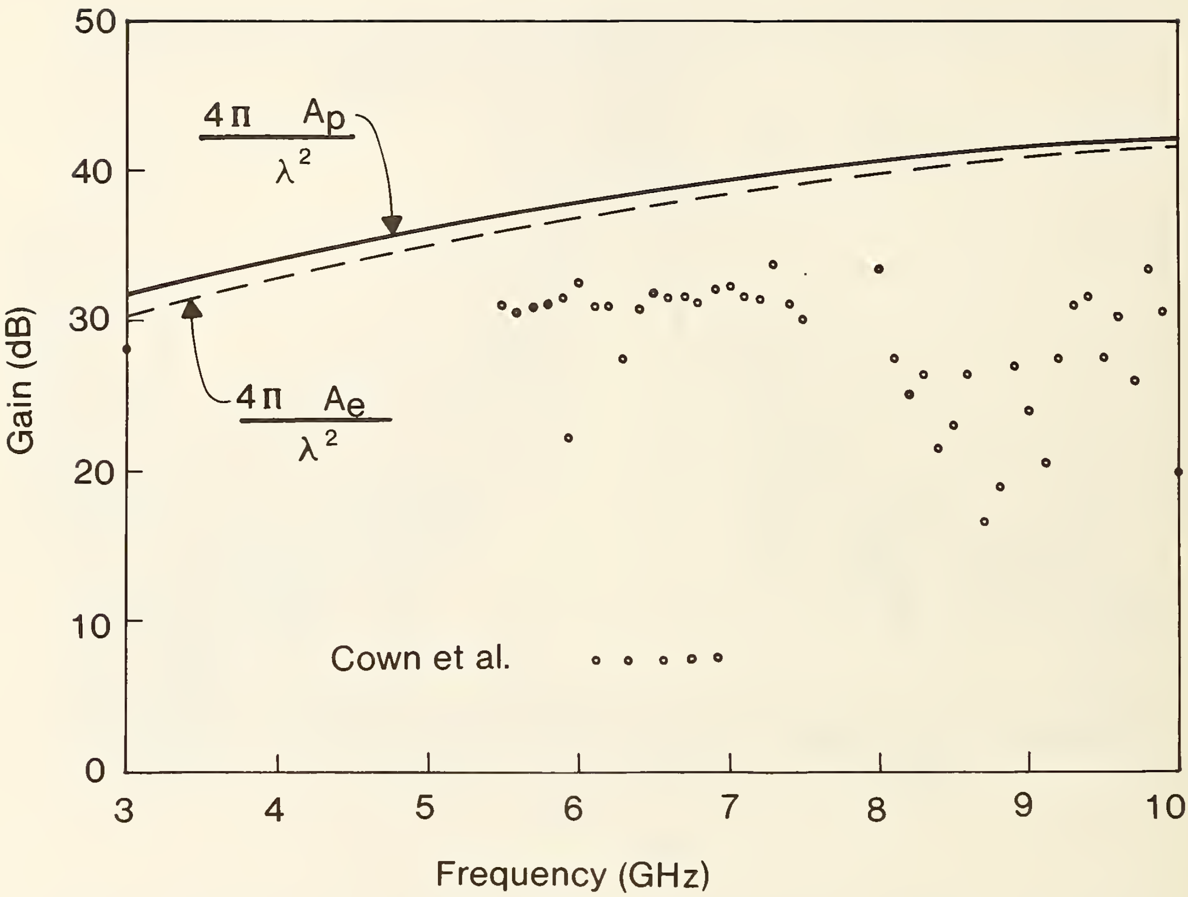

Figure 14. Comparison of theory and experiment [27] for gain as a function of frequency.

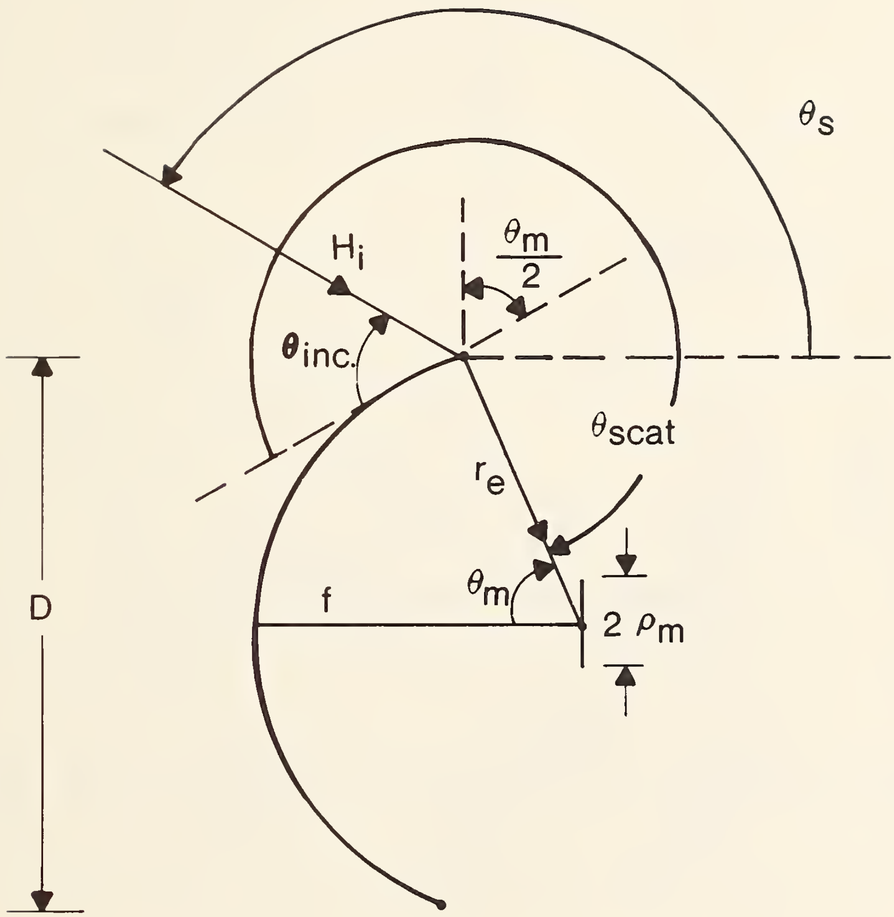

Figure 15. Geometry for diffraction from the edge of the reflector.

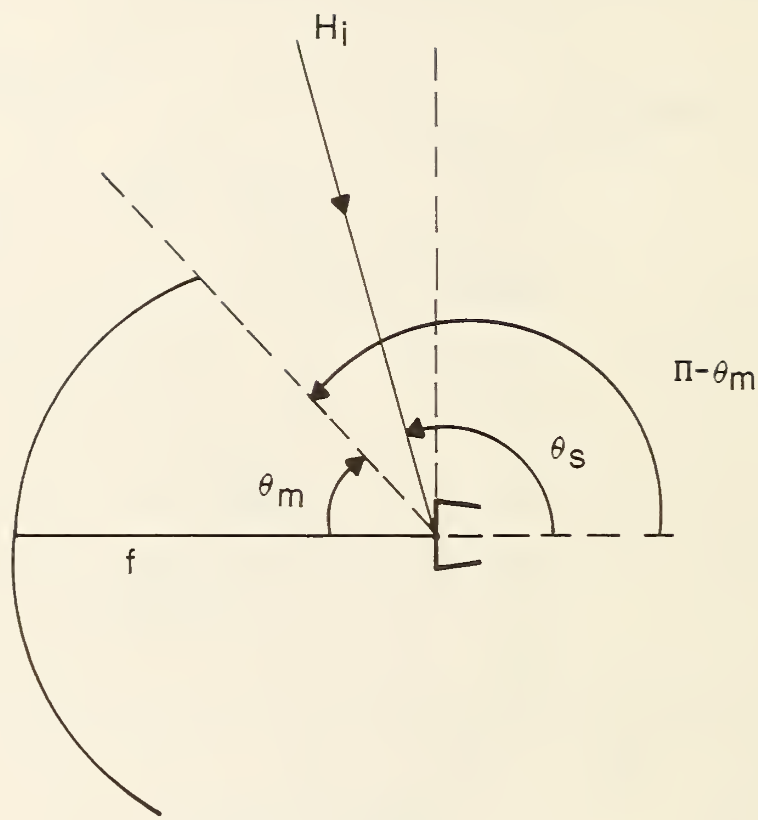

Figure 16. Geometry for direct illumination of the feed horn.

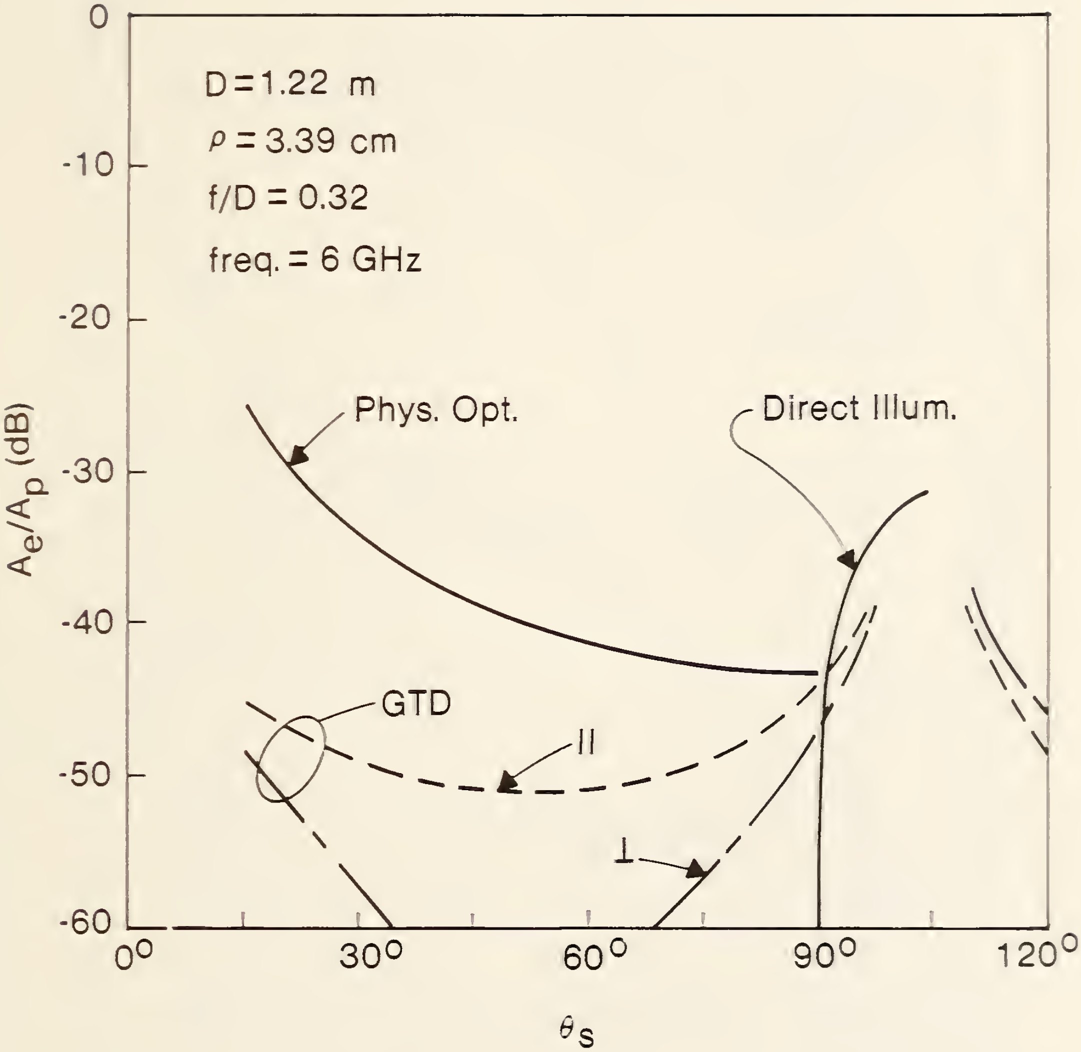

Figure 17. Various contributions to the wide angle receiving pattern.

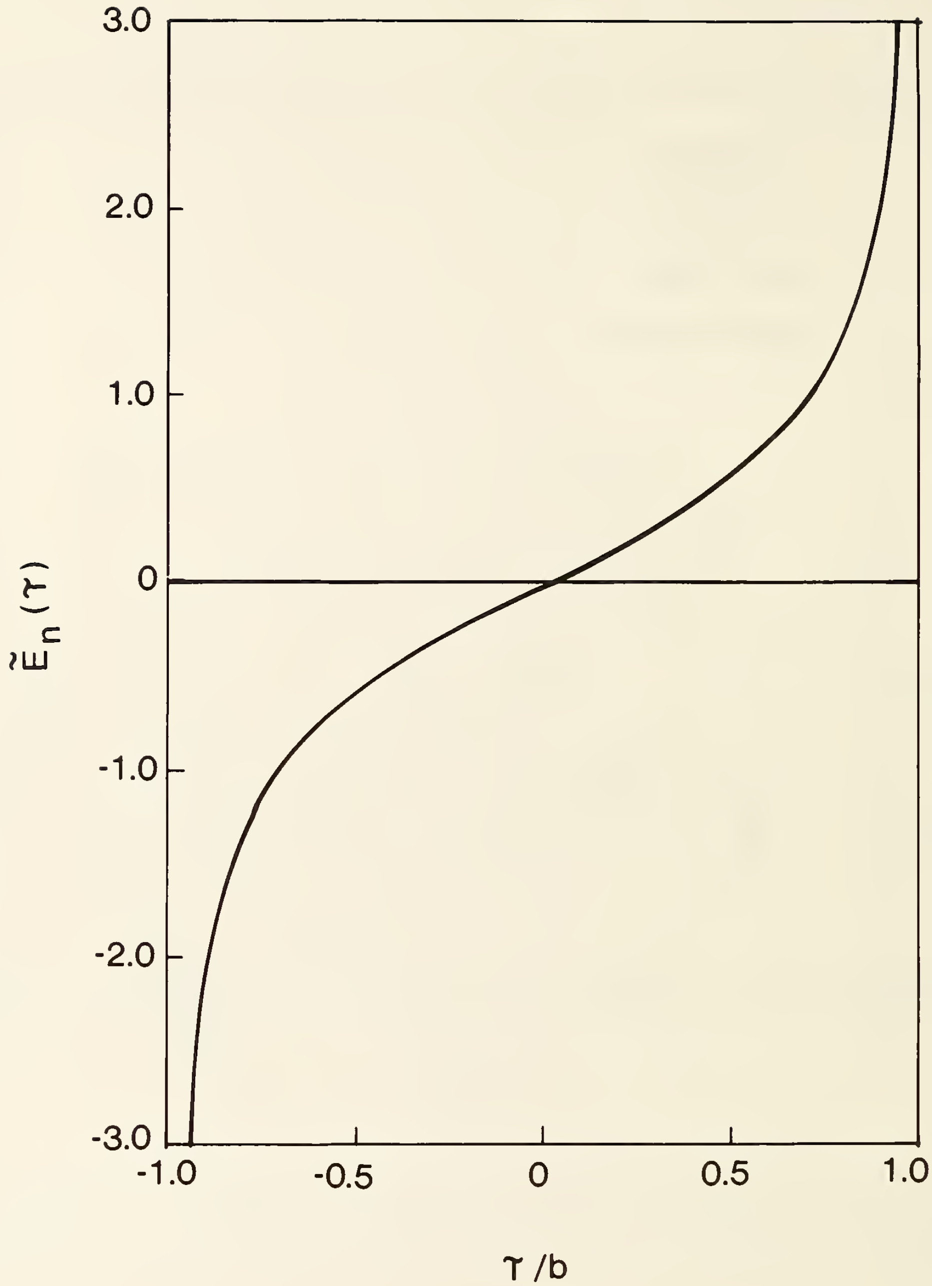

Figure 18. Normalized impulse response.

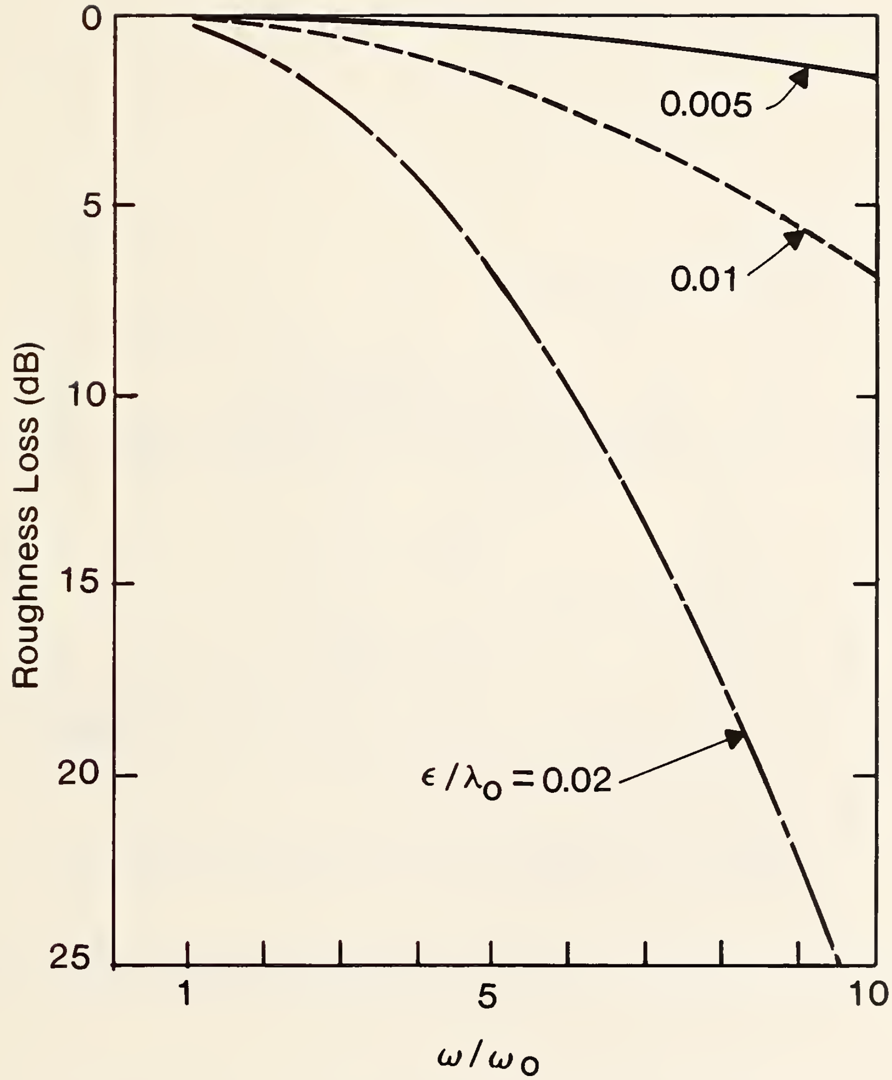

Figure 19. Roughness loss as a function of normalized frequency.

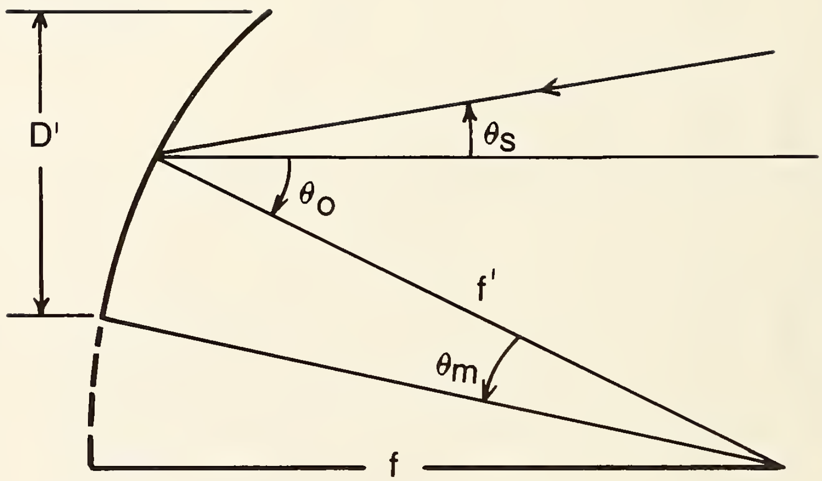

Figure 20. Geometry for an offset paraboloid.

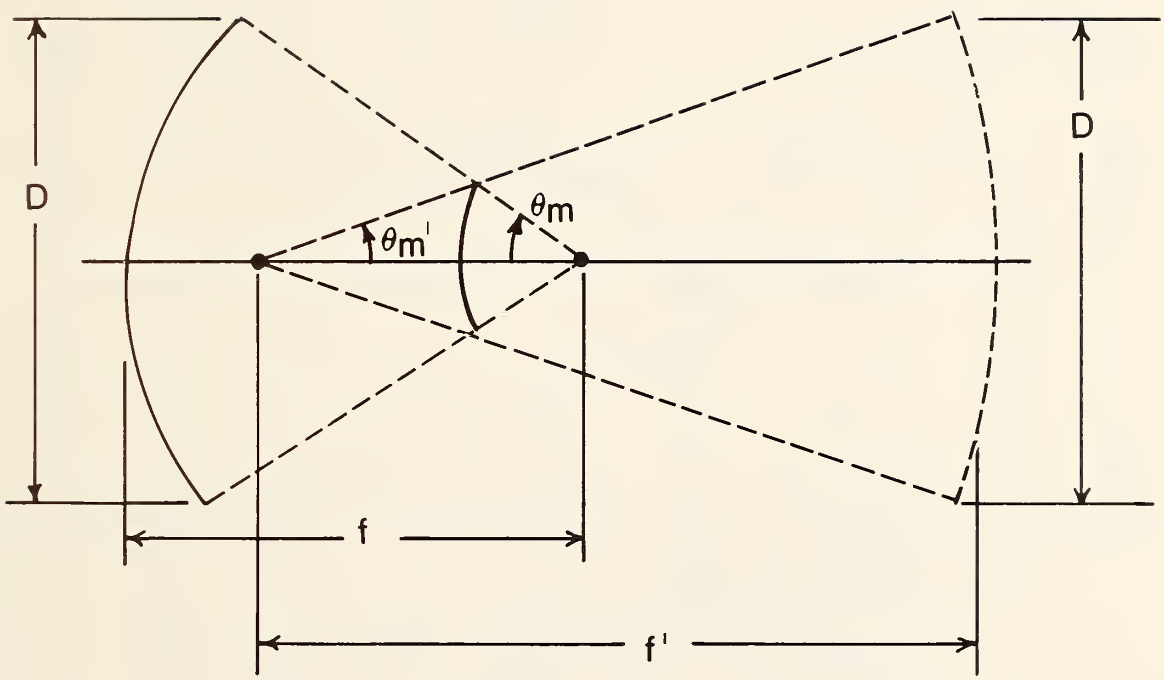

Figure 21. Geometry for a Cassegrain antenna. The equivalent paraboloid (dashed) has a focal length f'.

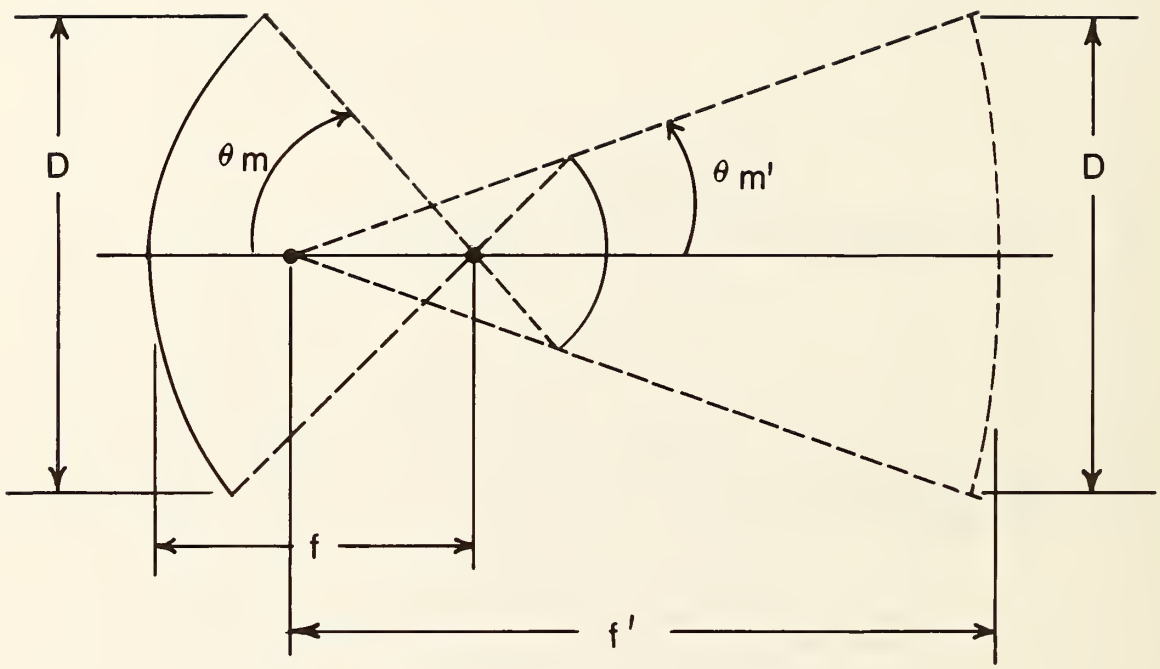

Figure 22. Geometry for a Gregorian antenna. The equivalent paraboloid (dashed) has a focal length f'.

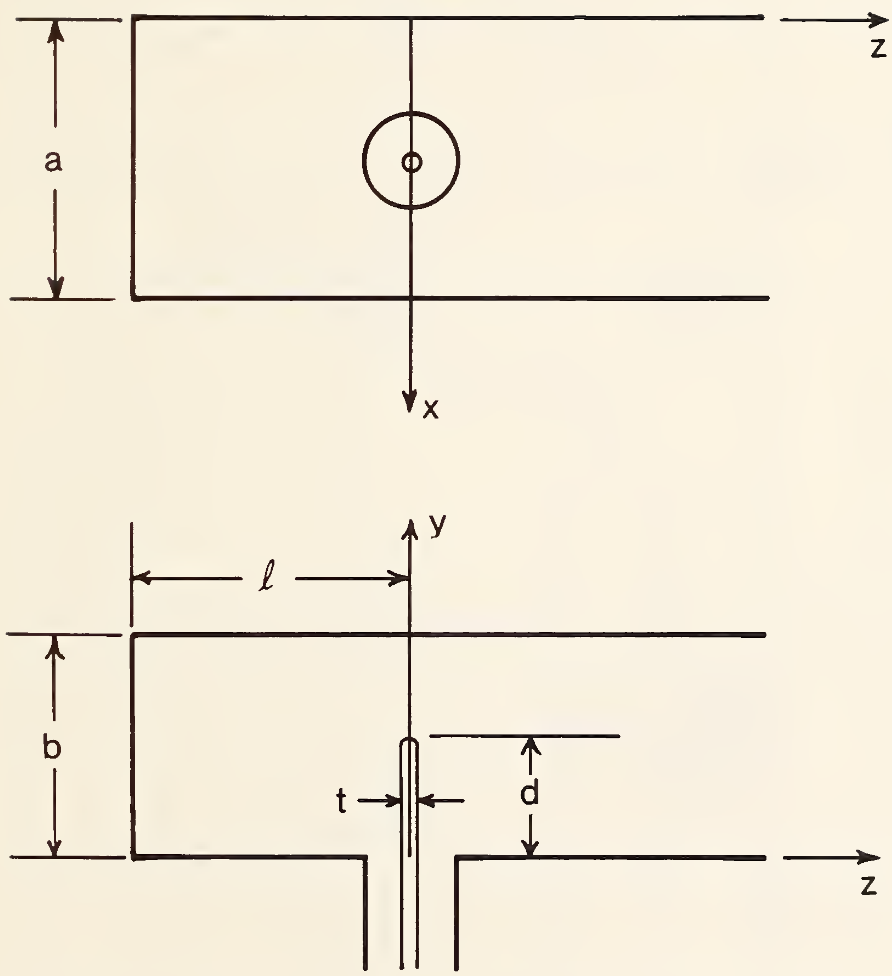

Figure 23. Probe type of coax-to-waveguide adapter.

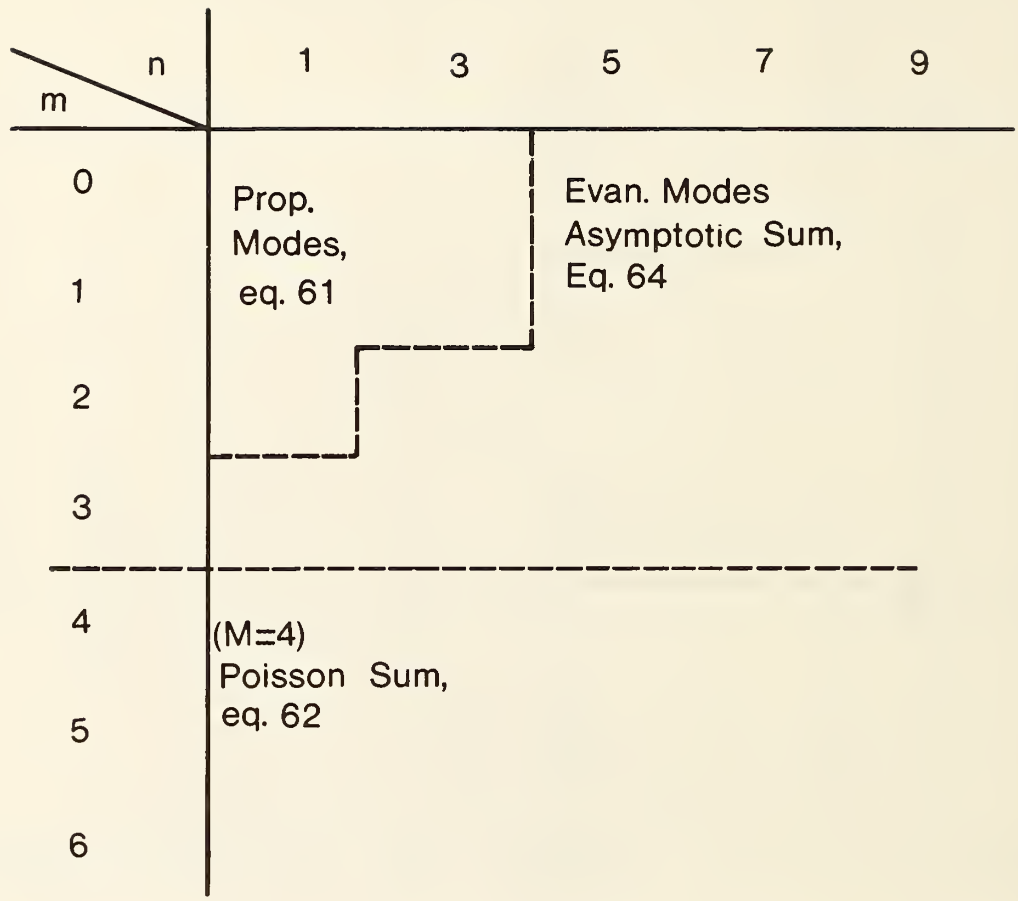

Figure 24. Computational scheme for evaluating Z_{in}. The nm modes are grouped into three regions: propagating modes, evanescent modes for $m < M$, and evanescent modes for $m \geq M$.

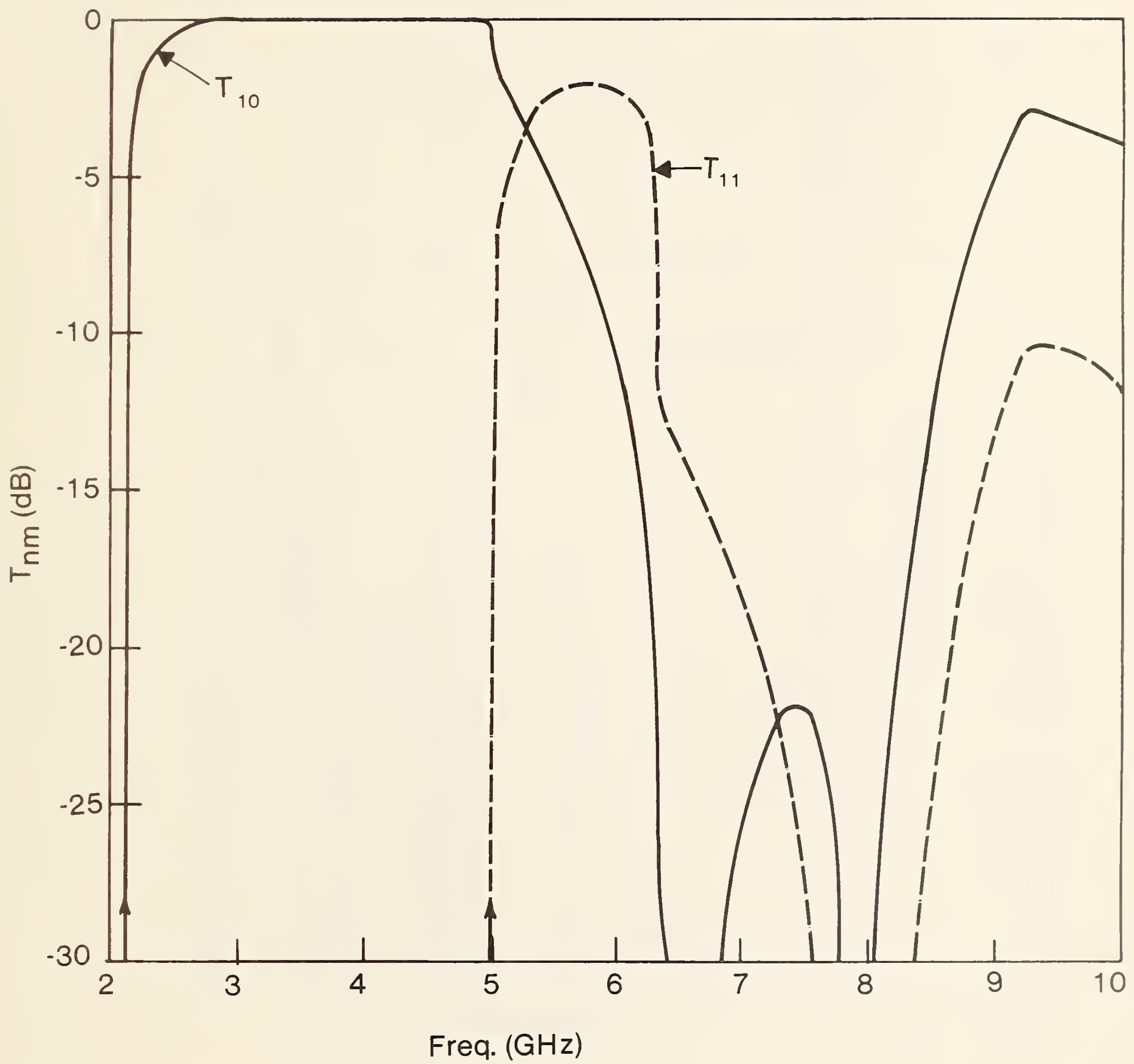

Figure 25. Transmission coefficients for an S-band coax-to-waveguide adapter. The cutoff frequencies for the dominant (TM^y_{10}) and first higher order (TM^y_{11}) modes are indicated by arrows.

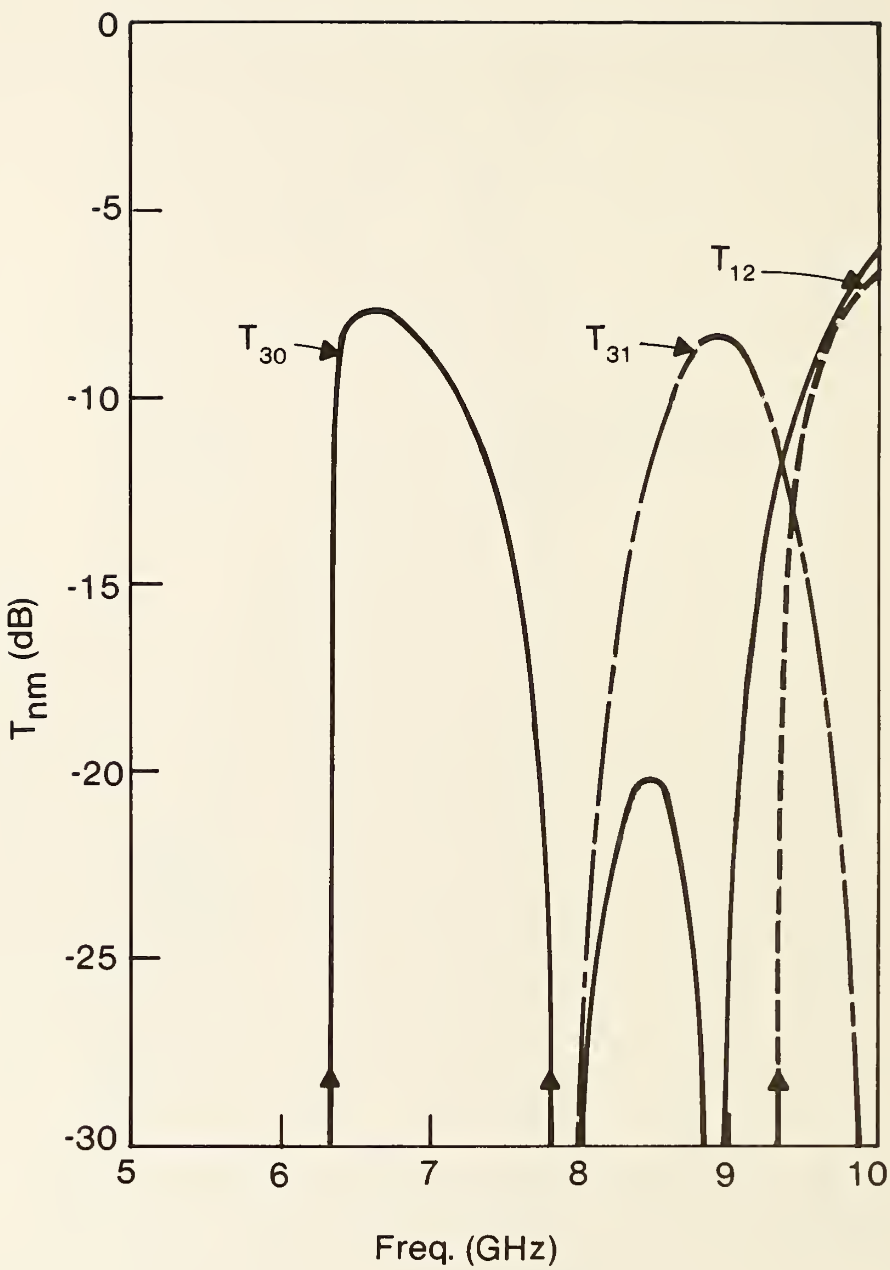

Figure 26. Transmission coefficients for the higher order modes of an S-band coax-to-waveguide adapter. The cutoff frequencies for the higher order waveguide modes are indicated by arrows.

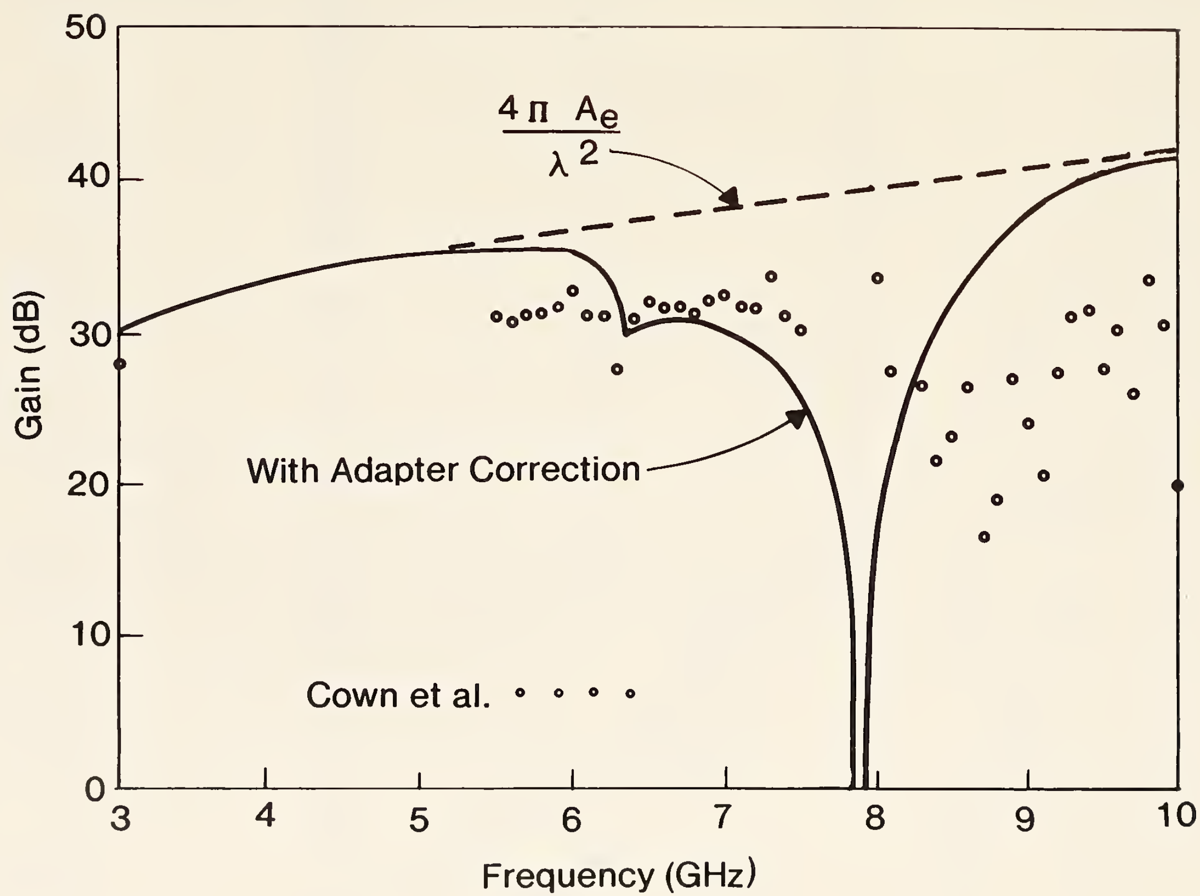

Figure 27. Comparison of theory (with adapter correction) and experiment [27] for antenna gain as a function of frequency.

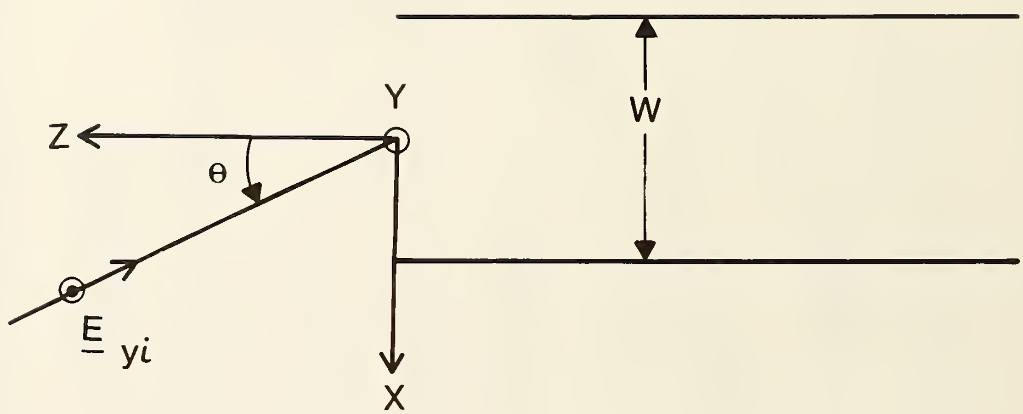

Figure 28. Plane wave incident on an open-ended, parallel-plate waveguide.

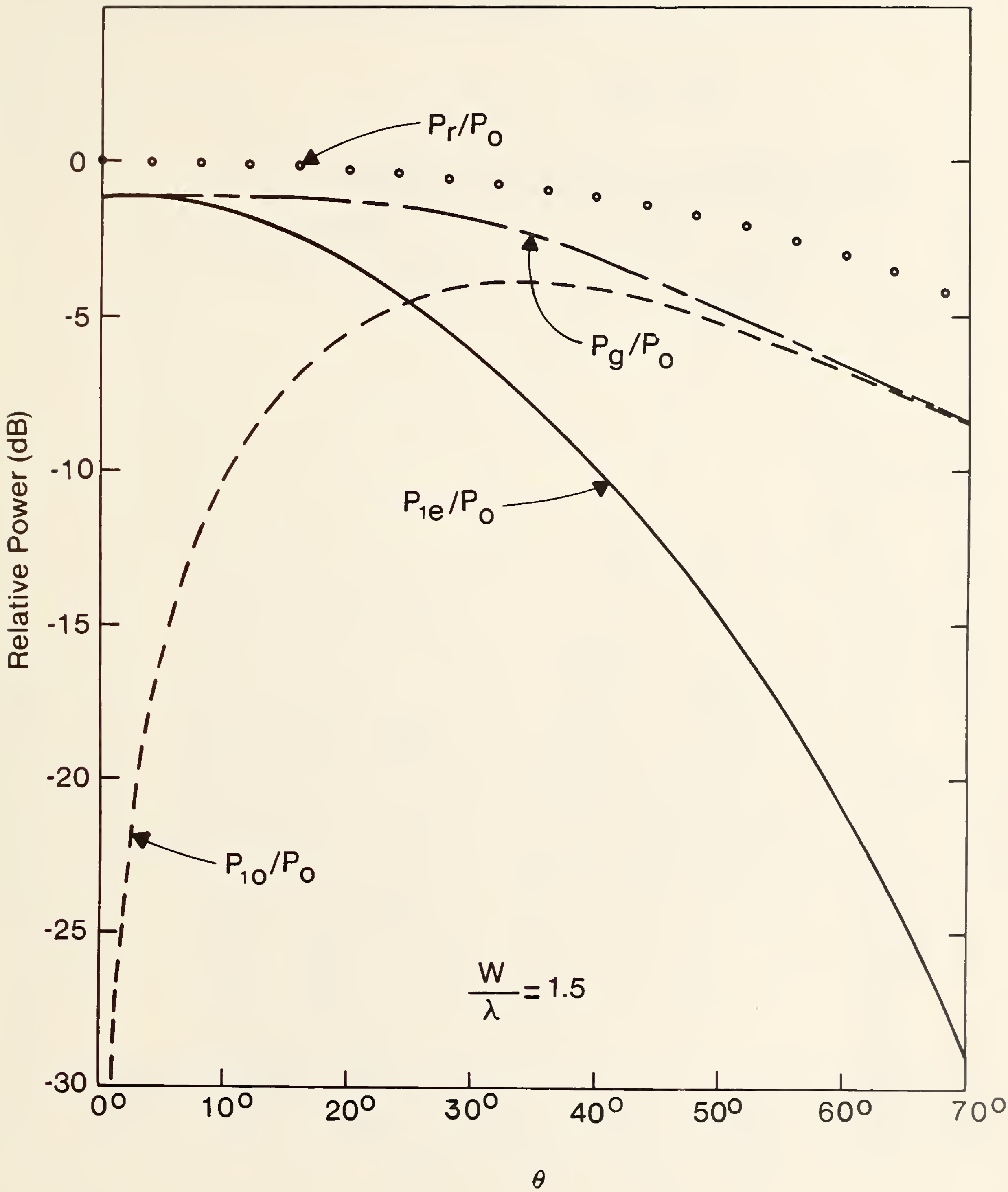

Figure 29. Total received power and the contributions from the n=1 even and odd modes. Only two modes are propagating.

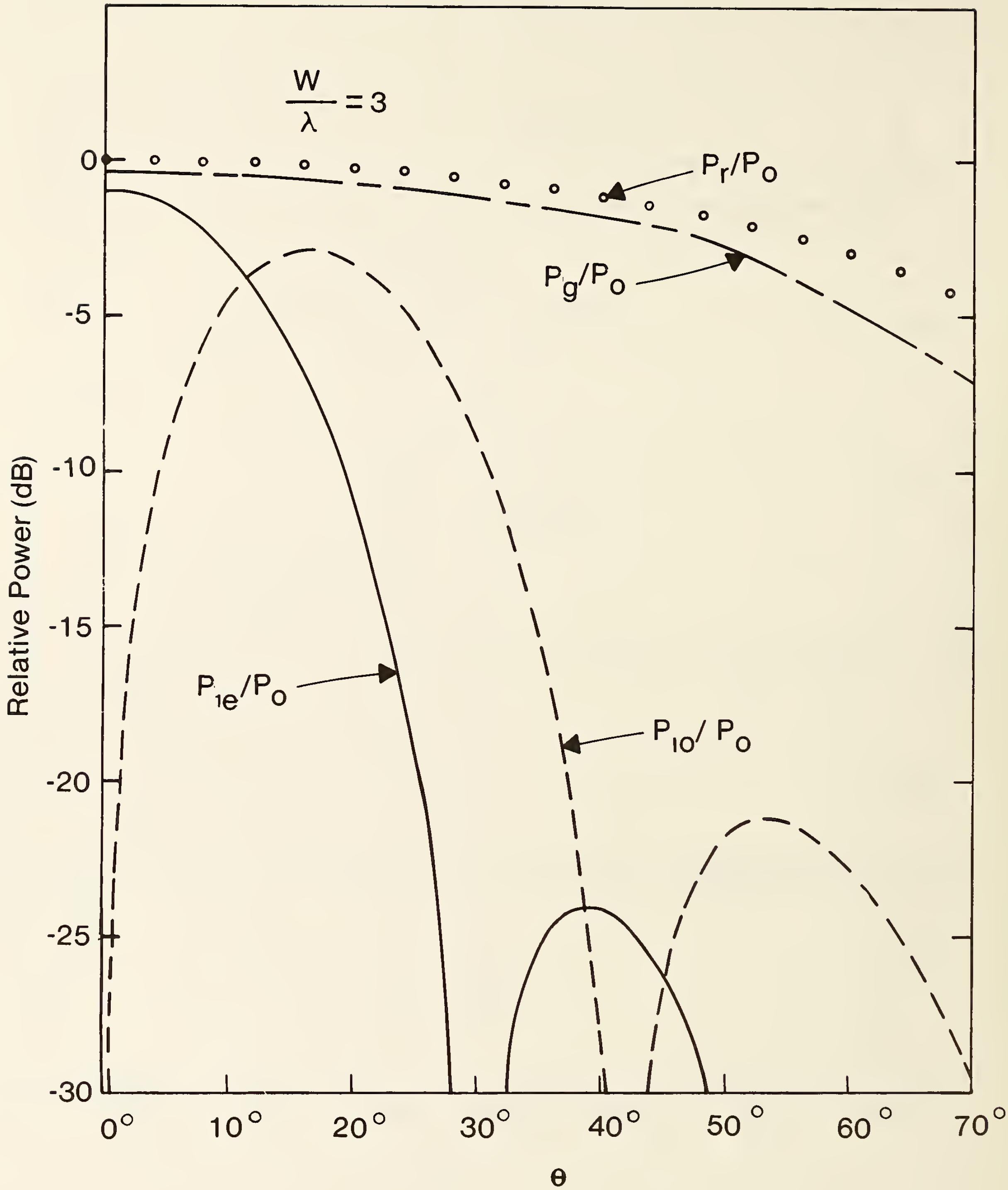

Figure 30. Total received power and the contributions from the n=1 even and odd modes. Five modes are propagating.

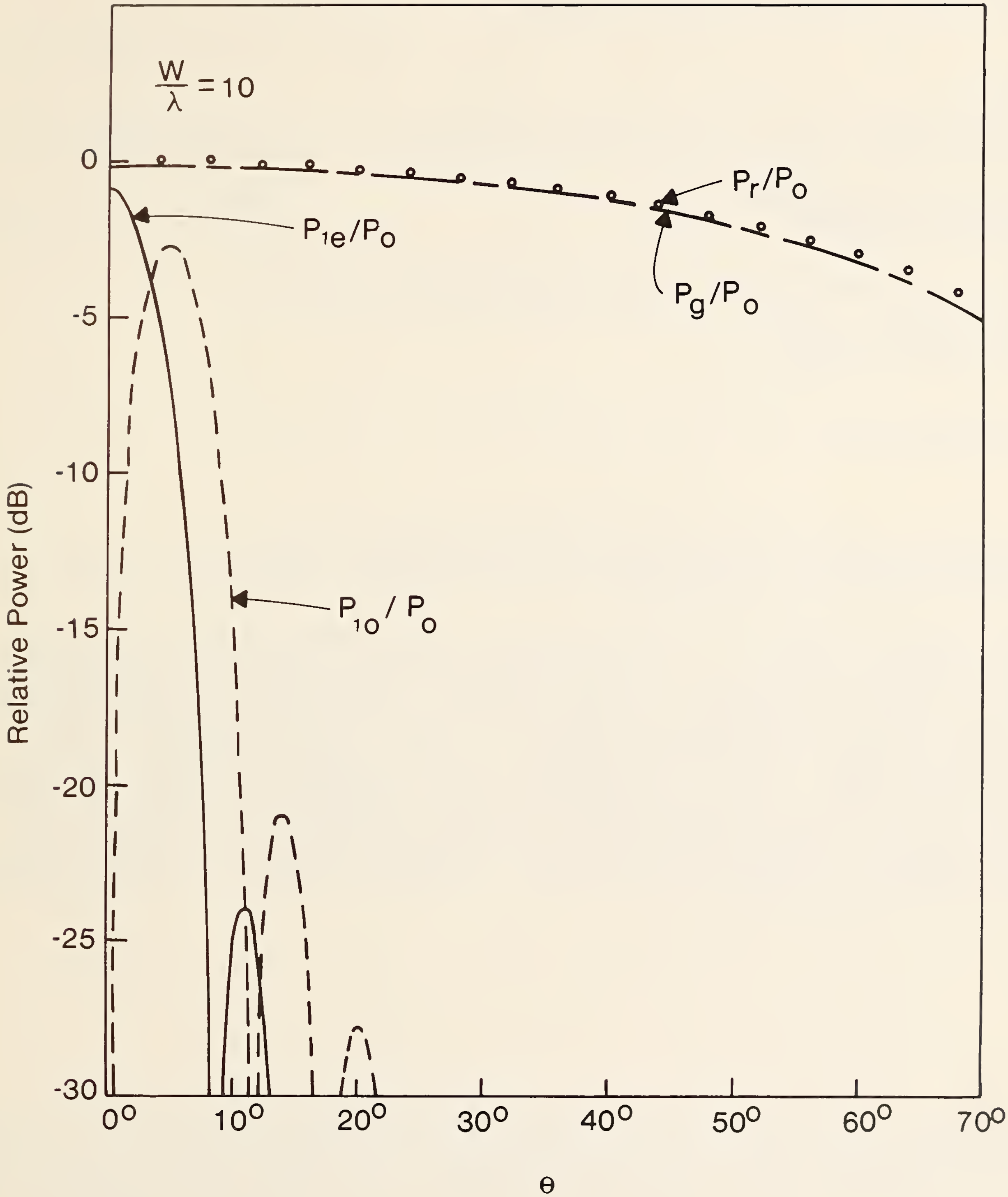

Figure 31. Total received power and the contributions from the n=1 even and odd modes. Nineteen modes are propagating.

NBS-114A (REV. 2-8C)

U.S. DEPT. OF COMM. BIBLIOGRAPHIC DATA SHEET (See instructions)	1. PUBLICATION OR REPORT NO. NBSIR 85-3021	2. Performing Organ. Report No.	3. Publication Date April 1985

4. TITLE AND SUBTITLE

Out-of-Band Response of Reflector Antennas

5. AUTHOR(S)

David A. Hill

6. PERFORMING ORGANIZATION (If joint or other than NBS, see instructions)

NATIONAL BUREAU OF STANDARDS
DEPARTMENT OF COMMERCE
WASHINGTON, D.C. 20234

7. Contract/Grant No.

8. Type of Report & Period Covered

9. SPONSORING ORGANIZATION NAME AND COMPLETE ADDRESS (Street, City, State, ZIP)

Defense Nuclear Agency
Washington, DC 20305

10. SUPPLEMENTARY NOTES

☐ Document describes a computer program; SF-185, FIPS Software Summary, is attached.

11. ABSTRACT (A 200-word or less factual summary of most significant information. If document includes a significant bibliography or literature survey, mention it here)

The response of reflector antennas to out-of-band frequencies has been analyzed using physical optics. A simple approximate expression has been obtained for the effective aperture, and this expression yields both the receiving pattern and the frequency dependence of the on-axis gain. The theory has been compared with published out-of-band measurements, and the pattern agreement is good, but the measured gain falls below the theory. This discrepancy is caused by mismatch loss in the coax-to-waveguide adapter, and this mismatch loss has been analyzed theoretically. The basic physical optics model for symmetrical reflectors has been extended to include offset and dual reflectors, reflector surface roughness, and transient excitation.

12. KEY WORDS (Six to twelve entries; alphabetical order; capitalize only proper names; and separate key words by semicolons)

coax-to-waveguide adapter; effective aperture; focal region; paraboloid, physical optics; Poynting vector; out-of-band response; receiving pattern; reflector antenna.

13. AVAILABILITY

☒ Unlimited
☐ For Official Distribution. Do Not Release to NTIS
☐ Order From Superintendent of Documents, U.S. Government Printing Office, Washington, D.C. 20402.
☒ Order From National Technical Information Service (NTIS), Springfield, VA. 22161

14. NO. OF PRINTED PAGES

76

15. Price

☆U.S. GOVERNMENT PRINTING OFFICE:1985—578-679 / 25186